# Experimental and Theoretical Evidence for Distorted Tetrahedral ≡Ti-OH Sites Supported on Amorphous Silica and Their Effect on the Adsorption of Polar Molecules

Branden E. Leonhardt<sup>1,2</sup>, Hengyuan Shen<sup>3</sup>, Martin Head-Gordon<sup>1,3</sup>, Alexis T. Bell<sup>1,2\*</sup>

<sup>1</sup>Chemical Sciences Division, Lawrence Berkeley National Laboratory, Berkeley, California 94720, USA <sup>2</sup>Department of Chemical and Biomolecular Engineering, University of California, Berkeley 94720, USA; <sup>3</sup>Department of Chemistry, University of California, Berkeley 94720, USA;

<sup>\*</sup>To whom correspondence should be sent: <a href="mailto:alexbell@berkeley.edu">alexbell@berkeley.edu</a>

## **Abstract**

This study presents experimental and theoretical evidence for distorted ≡Ti-OH groups supported on amorphous SiO2 and examines the influence of distortion on the strength of adsorption of polar molecules. For the theoretical part of this effort, we developed a model for isolated ≡Si-OH or ≡Ti-OH groups on the surface amorphous silica. The ≡M-OH group is represented by a T8-10 cluster surrounded by a T747 cluster representing the surrounding amorphous silica. The properties of the small cluster are described by high-level density functional theory (DFT) (i.e. the quantum mechanical (QM) region), whereas the large surroundings is represented by molecular mechanics (MM). The QM/MM model was validated by demonstrating that the predicted enthalpy of adsorption for a number of polar molecules on ≡Si-OH groups agrees satisfactorily with experimentally measured values determined by microcalorimetry. We also found that enthalpies of adsorption on isolated ≡Si-OH groups determined from isotherms obtained by IR spectroscopy agree very well with the microcalorimetric values. IR spectroscopy was then used to measure isotherms for pyridine adsorption to Lewis acidic Ti isolated ≡Ti-OH groups grafted to amorphous silica. The isosteric enthalpy of adsorption determined by this means was found to decrease in magnitude with increasing pyridine coverages up to a coverage of 15% and to then be relatively constant for higher coverages. QM/MM calculations made with our model revealed that the enthalpy of adsorption is proportional to the area of the triangular O-Ti-O facets of the ≡Ti-OH group to which pyridine is bound. ≡Ti-OH sites exhibiting facet areas consistent with those deduced from X-Ray Absorption Spectroscopy (XAS/EXAFS) measurements bind pyridine with enthalpies of adsorption consistent with the observed plateau for pyridine coverage above 15%. Larger tetrahedral facet areas are required to explain the coverage-dependent enthalpies of adsorption below 15% coverage, evidencing distorted ≡Ti-OH structures. Distorted ≡Ti-OH sites are also qualitatively consistent with reduced-intensity pre-edge X-Ray Absorption Near Edge Structure (XANES) measurements reported in this study. Energy decomposition analysis (EDA) calculations were carried out to understand the underlying physical phenomenon governing the change in the enthalpies of adsorption pyridine as a function of tetrahedral facet area.

Keywords: adsorption, silica, titanium, DFT, catalysis

## Introduction

Silica-supported metal cations (SSMCs), such as Ti, Cr, W, Mo, Zr, V, and Nb are widely used as catalysts to promote industrially relevant chemical reactions, such as alkene epoxidation, alkene polymerization, and alkene metathesis. 1-9 At low metal loadings, metal cations are present as isolated species (e.g., ≡M-OH, =M(O)₂) grafted to the surface of silica through covalent M-O-Si bonds (where M = Ti, Cr, W, etc.). Recent experimental and computational studies suggest that the distribution of O-Si-O bond angles amorphous silica can distort the structure of the supported  $\equiv$ M-OH and =M(O)<sub>2</sub> species, thereby affecting their adsorptive and catalytic properties. <sup>10,11</sup> Although the catalytic relevance of distortion of these species has been reported for over a decade, many recent computational studies have assumed relatively symmetrical metal sites to compute the enthalpy landscape on which reactions occur. 5,6,12-15 Furthermore, these models typically assume the structure of a corner-substituted silsesquioxane. While such a model is computationally efficient, it neglects non-local interactions between the adsorbate and the surrounding silica support. Therefore, it is not known whether silsesquioxane-based models of silica are accurate when used to compute adsorption enthalpies. This is an important question given the extensive theoretical work on microporous-silica and zeolites, which have concluded that small cluster models are generally insufficient because they neglect long-range electrostatic and short-range van der Waals (VDW) interactions between the surrounding silica of the micropore and the adsorbate. 16,17 Thus, the successful application of theory to the investigation of supported =M-OH and =M(O)<sub>2</sub> species requires the identification of a physically meaningful representation for SSMCs that can then be used to determine what effects geometrical distortions of their structure have on their adsorptive and catalytic properties.

In this study, we explore alternative representations of amorphous silica in theoretical studies of the adsorption of polar molecules on silanol (≡Si-OH) groups and isolated titanol (≡Ti-OH) groups supported on the surface of amorphous silica. Silanol groups are considered because of the large body of experimental work concerning the enthalpy of adsorption of polar molecules on such groups. 18-24 The reason for choosing ≡Ti-OH groups is that they have been the subject of many experimental and theoretical studies. 6,25-28 We also examine whether distortion of the geometry of ETi-OH groups affects the enthalpy of adsorption of polar molecules on these groups. To address these questions, we have explored the influence of cluster size on the predicted enthalpies of adsorption for polar molecules interacting with isolated ≡Si-OH groups and their agreement with microcalorimetric measurements. To investigate the adsorption of polar molecules on silica-supported ≡Ti-OH groups, we prepared a sample of Ti/SiO₂ and confirmed experimentally that all Ti was dispersed as isolated =Ti-OH groups. We then used IR spectroscopy of adsorbed pyridine to obtain adsorption isotherms from which the isosteric enthalpies of adsorption could be determined. This experimental approach was validated by demonstrating that the enthalpy of adsorption for polar molecules adsorbed on ≡Si-OH groups is consistent with the value determined by microcalorimetry. Ultimately, we used our IR approach to identify that the enthalpy of pyridine adsorption on isolated ≡Ti-OH groups is coverage dependent and to demonstrate that our theoretical approach shows that the variation of the isosteric enthalpy of adsorption of pyridine,  $\Delta H_{ads}^o$ , is a consequence of the geometric distortion of a portion (~15%)

of the supported  $\equiv$ Ti-OH groups. Physical insights into how distortion impacts  $\Delta H_{ads}$  of pyridine were obtained by carrying out an energy decomposition analysis (EDA).<sup>29</sup>

# Methods

## Silica preparation

Fumed silica, an amorphous, non-porous material was obtained from Sigma Aldrich (surface area = 395 m²/g  $\pm$  25 m²/g). All samples underwent consistent pre-treatment to ensure reproducibility. First, the raw material was dispersed into boiling water (1:1 by volume) for 24 h (with constant stirring), cooled, and filtered. The silica cake was dried in an oven at 353 K under nitrogen overnight to form silica chips. The chips were ground in a mortar and pestle and sieved to a consistent particle size (250  $\mu$ m <  $\varphi$ d < 500  $\mu$ m). This sample will be termed SiO<sub>2,Hyd</sub> due to its subjection to hydroxylation procedures. SiO<sub>2,Hyd</sub> was heated in 100 mL/min of Praxair Extra Dry air at 1023 K (3 K/min ramp rate) for 8 h and cooled to room temperature (SiO<sub>2-1023</sub>).

## Thermogravimetric Analysis (TGA) to determine silanol density

TGA was conducted using a TGA Q5000 instrument equipped with a high-temperature platinum or ceramic crucible. All sample mass thermograms were corrected for buoyancy effects by subtracting the mass thermogram of an empty pan with an identical thermal program. To determine the silanol density, ~10-20 mg of silica was heated in a flow of 100ml/min air (Praxair UHP air) to 383 K at 5 K/min and held at this temperature for 1h, followed by heating to 1273 K at 5 K/min. To calculate the silanol density, equation (1) was used.

Silanol density 
$$\left(\frac{OH}{nm^2}\right) = \frac{2(\Delta m_{TGA})N_{Avogadro}}{M_{H_2O}A_{BET}}$$
 (1)

where  $\Delta m_{TGA}$  is the cumulative mass loss between the stable mass at 383 K and the final mass at 1273 K in grams,  $M_{H_2O}$  is the molar mass of water in g/mol,  $N_{Avogadro}$  is Avogadro's number,  $A_{BET}$  is the BET surface area in nm², and the factor of 2 accounts for the fact that every molecule of water evolved comes from the condensation of two silanol groups.  ${\bf SiO}_{2,Hyd}$  was found to contain  $4.8\pm0.1$  OH/nm² from this method (Figure S1), which is in excellent agreement with Zhuravlev et al. for fully hydroxylated silica materials.<sup>30</sup> Using the same method,  ${\bf SiO}_{2-1023}$  was found to contain 1.4 OH/nm², which is within the expected range after the thermal treatment employed (Figure S2).<sup>30</sup>

## Wet impregnation of SiO<sub>2-1023</sub> with Cp<sub>2</sub>TiCl<sub>2</sub> and calcination to form Ti/SiO<sub>2-1023</sub>

Ti was grafted onto the surface of  $SiO_{2-1023}$  using  $Cp_2TiCl_2$  (Strem Chemicals) as the Ti precursor. This step was conducted under air-free conditions utilizing an  $N_2$  Schlenk line.  $^{31}$   $N_2$  was supplied at 10 psig from a cylinder (Praxair) and passed over a Vici Valco  $N_2$  purifier prior to use in the Schlenk line. First,  $SiO_{2-1023}$  was charged to a three-neck flask connected to a Schlenk filter, a septum, and a glass stopper. The flask was evacuated and back-filled with  $N_2$  three times. Then, the sample was dehydrated for 2 h under dynamic vacuum ( $10^{-1}$  mbar) at  $503 \pm 20$  K at 10-20 K/min using a sand bath. Meanwhile, the desired amount of  $Cp_2TiCl_2$  was charged to a separate three-neck flask connected to the Schlenk line, a Schlenk funnel, and a septum. The flask was also

evacuated and back-filled with  $N_2$  three times. Then, it was left under dynamic vacuum ( $10^{-1}$  mbar) for 2 h. Next, 60 mL of anhydrous chloroform was added to the titanium precursor (now under  $N_2$ ) and was allowed to stir for 1 h. After cooling the silica to room temperature, the vessel was filled with dried  $N_2$  and the titanium precursor/chloroform solution was transfer to the silica via a cannula. The suspension was stirred and allowed to react for 2 h, after which the entire glassware setup was rotated  $180^\circ$  and the liquid suspension was passed through a Schlenk filter. Finally, residual chloroform was removed by evacuation for 1 h into a liquid  $N_2$  trap placed upstream of the vacuum pump to leave a milky orange powder ( $SiO_{2-CP}$ ). At this point, the sample was exposed to ambient conditions and immediately calcined in air (Praxair Extra Dry) at 823 K (3 K/min ramp rate) for 8 h producing a bright white powder ( $Ti/SiO_{2-1023}$ ).

## Synthesis of Ti[SiOPh<sub>3</sub>]<sub>4</sub>

The synthesis of  $Ti[SiOPh_3]_4$  was carried out following the procedure of Johnson et al. <sup>32</sup> Briefly, 2 g of Ph<sub>3</sub>SiOH (Sigma-Aldrich) was charged to a Schlenk flask inside a N<sub>2</sub>-purged glovebox. The flask was sealed and transferred to a Schlenk line where it was evacuated and purged with filtered N<sub>2</sub> three times. Then, 50 mL of toluene (Fischer Scientific) was cannula transferred to the Schlenk flask containing Ph<sub>3</sub>SiOH and the solution was stirred for 10 minutes. Finally, 0.47 mL of  $Ti(OBu^n)_4$  was added to the now-stirring solution (700 rpm). The product,  $Ti[SiOPh_3]_4$ , precipitated out immediately. The solution was detached from the Schlenk line and vacuum-filtered overnight to leave a bright white powder. The structure of  $Ti[SiOPh_3]_4$  was confirmed by X-ray absorption spectroscopy (Figure S3).

## N<sub>2</sub> Physisorption measurements

BET surface areas were calculated from  $N_2$  physisorption isotherms measured at 77 K using a Micromeritics Gemini VII surface area and pore volume analyzer. The BET surface area for  $SiO_{2,Hyd}$  and  $SiO_{2-1023}$  was 335 and 334 m²/g respectively. Both samples display IUPAC Type 2  $N_2$  adsorption isotherms consistent with a non-porous material (Figure S4). The measured BET surface area for  $Ti/SiO_{2-1023}$  was 298 m²/g. Prior to isotherm measurement, samples were treated at 403 K under vacuum.

## Diffuse Reflectance UV/Visible Spectroscopy (UV/Vis)

UV/Vis spectra were acquired on a Thermo Scientific Evolution 3000 UV/Vis spectrophotometer equipped with a Harrick Praying Mantis Diffuse Reflectance accessory. Reference spectra were acquired with BaSO<sub>4</sub> and transformations from percent reflectance to absorbance were calculated with the Kubelka-Munk function. Samples were heated under 100 ml/min of flowing He (Praxair UHP grade) to 673 K (6.25 K/min ramp rate), held at 673 K for 1h, then cooled to the conditions of interest. The UV/Vis spectrum of SiO<sub>2-1023</sub> was subtracted from that of Ti/SiO<sub>2-1023</sub>. To make a quantitative comparison with the literature, Tauc plots were constructed assuming direct transitions, and the direct edge energy was calculated using a sigmoidal fitting procedure as in previous work.<sup>33</sup>

## Fourier-Transform Infrared Spectroscopy (FTIR)

Catalyst samples (~30 mg) were pressed into self-supporting pellets and loaded into a stainless-steel sample holder that was then placed in a home-built in-situ transmission IR cell. The cell was

connected to heated stainless-steel gas transfer lines. A septum adapter was placed upstream of the cell, allowing for continuous liquid injection (Legato 100 syringe pump) into the heated gas stream. The *in-situ* cell was equipped with a cylindrical heater, and the temperature was measured using a K-type thermocouple (Omega) in direct physical contact with the stainless-steel sample holder. The temperature was controlled using an Omega CS8DPT controller. Spectra were acquired using a Thermo Scientific Nicolet 6700 FTIR spectrometer with a liquid-nitrogen-cooled MCT detector.

All FTIR measurements followed the same sample pretreatment conditions. Samples were heated under 100 ml/min of flowing He (Praxair UHP grade) to 673 K (6.25 K/min ramp rate), held at 673 K for 1h, then cooled to the conditions of interest. For isotherm measurements, pyridine (Sigma-Aldrich), acetone (Sigma-Aldrich), and  $d_3$ -acetonitrile (Sigma-Aldrich) were injected into the heated He gas stream at a flowrate needed to obtain the desired partial pressures. The liquid injection rate was modified while the He flowrate was kept constant to accomplish this. Equilibration was determined when the area of the IR band corresponding to adsorbed pyridine, acetone, or  $d_3$ -acetonitrile no longer changed, which typically occurred within 3 min. All spectra were collected as an average of 64 scans with 1 cm<sup>-1</sup> resolution.

Peak deconvolution and fits were performed with Origin software. For pyridine adsorption experiments, ring-breathing vibrational absorbance features were numerically integrated after baseline subtraction. For d<sub>3</sub>-acetonitrile, acetone, and trimethylacetonitrile, peaks were fit to the spectra. For d<sub>3</sub>-acetonitrile and trimethylacetonitrile, we fit Gauss-Lorentz functions with 80% and 50% Lorentzian weights, respectively, as these provided the best fits to our data. Others have found these line shapes to fit spectra of CD<sub>3</sub>CN adsorbed to Sn and Zn sites within zeolites.<sup>34</sup> These weights were kept fixed for all conditions. Peak centers and full-width half-maximums (FWHM) were allowed to vary freely, but did not change by more than 2 cm<sup>-1</sup> for both parameters. For acetone, two Lorentz line shapes were fit to the spectra to represent two distinct adsorbed species.<sup>35</sup> Peak centers were kept fixed at 1712 cm<sup>-1</sup> and 1699.5 cm<sup>-1</sup> with FWHM fixed at 16 cm<sup>-1</sup> and 20.1 cm<sup>-1</sup>, respectively, for all conditions. The magnitudes and trends of the FWHM reported here for both components are consistent with others.<sup>35</sup>

## X-ray absorption spectroscopy (XAS)

XAS spectra at the Ti K-edge were acquired on beamline 10-BM at the Advanced Photon Source at Argonne National Laboratory. The energy was referenced to Ti foil (4966 eV) taken in transmission mode. Before measurement, Ti[SiOPh<sub>3</sub>]<sub>4</sub> was diluted with boron nitride. The XAS of Ti/SiO<sub>2-1023</sub> was acquired in fluorescence mode using a Vortex detector and an in-situ cube cell. Multiple spectra were merged to improve the signal-to-noise ratio as much as reasonably possible. Data was collected from 4780 eV to 5767 eV with a step size of 0.1 eV in the pre-edge region. Due to the low loadings of Ti in Ti/SiO<sub>2-1023</sub> samples, the EXAFS region of the XAS yielded low signal, so only pre-edge data was acquired. All data workup and analysis were conducted using Athena and Artemis.<sup>36</sup> After background subtraction, all spectra were normalized to the absorbance in the region 150-400 eV above the edge. Pre-edge features were baseline corrected using an arctan function, as reported previously.<sup>28</sup> An EXAFS fit for Ti[SiOPh<sub>3</sub>]<sub>4</sub> was performed in

the range 1.2-2.2 Å in R-space. Initial guesses for Ti-O scattering paths were calculated from the crystal structures of **Ti[SiOPh<sub>3</sub>]**<sub>4</sub> using the FEFF6 plug-in within Artemis.<sup>32,36</sup>

#### QM/MM and QM calculations

All geometry optimizations and frequency calculations (to confirm minima on the potential energy surface) for all structures were performed with  $\omega$ B97X-D/def2-SVP. Single-point energy calculations, used for calculating  $\Delta H_{ads}^o$ , were performed with  $\omega$ B97M-V/def2-TZVP. The larger basis set and more advanced functional yield statistically higher quality interaction energies. All electronic structure calculations employed the pruned SG-3 (99, 590) quadrature grid. In the larger and entropy corrections at a given temperature used a quasi-rigid rotor harmonic oscillator model (qRRHO). In cases where multiple local minima were found for the same adsorption phenomenon, (i.e. pyridine adsorption to an isolated silanol), the  $\Delta H_{ads}^o$  was calculated by a Boltzmann weighted average. Boltzmann factors were calculated using estimated  $\Delta G_{ads}^o$  for each optimized geometry.

The T8 silsesquioxane, as well as models B and C in Figure 1 (below) were standard DFT calculations (i.e., full QM). For larger models, such as D, E, and F, Quantum-mechanics/Molecular Mechanics (QM/MM) calculations were performed using the P2 set of MM parameters.<sup>41</sup> This methodology defines a QM region on the silica surface that includes the central ≡Ti-OH/≡Si-OH site along with a small number of surrounding silica atoms. We extended the QM region out to the next-next nearest neighbor Si atom from the central ≡Ti-OH/≡Si-OH site, thus the QM region was typically 8-11 tetrahedral atoms (T-atoms) large. The QM region also includes all adsorbate atoms and electrons. For example, the QM region for the ≡Si-OH site is shown in panel C of Figure 1, while panels D, E, and F, show progressively larger MM regions. This methodology assumes the MM region is included in the DFT Kohn-Sham equation as point charges, the values of which are part of the P2 set of parameters. 41 Since MM parameters were not developed for silanol groups in the MM region, all silanols (OH groups) were replaced as terminal H atoms which are modeled as boundary O atoms in the QM/MM formalism.<sup>41</sup> Additionally, adsorbate atoms and MM region atoms interact via a pairwise VDW potential modeled by a standard Lennard-Jones function. The Lennard-Jones function uses the P2 parameters for the MM region developed previously for all siliceous-zeolites<sup>41</sup>, while adsorbate atoms take on their parameters as listed in the CHARMM database. All computations were performed using the Zeolite package within Q-Chem version 5.43

## Models for SiO<sub>2</sub> and Ti/SiO<sub>2</sub>

Two categories of models for SiO<sub>2</sub> were examined. The first was a small cluster model (T8 silsesquioxane) that has been used frequently to model silica and silica-supported metals for catalytic reactions.<sup>5,6,12–15,44</sup> We next considered progressively larger models of amorphous silica taken from the structure of this material generated by Tielens et al.<sup>45,46</sup> Representative images of each type of model we considered are shown in Figure 1.

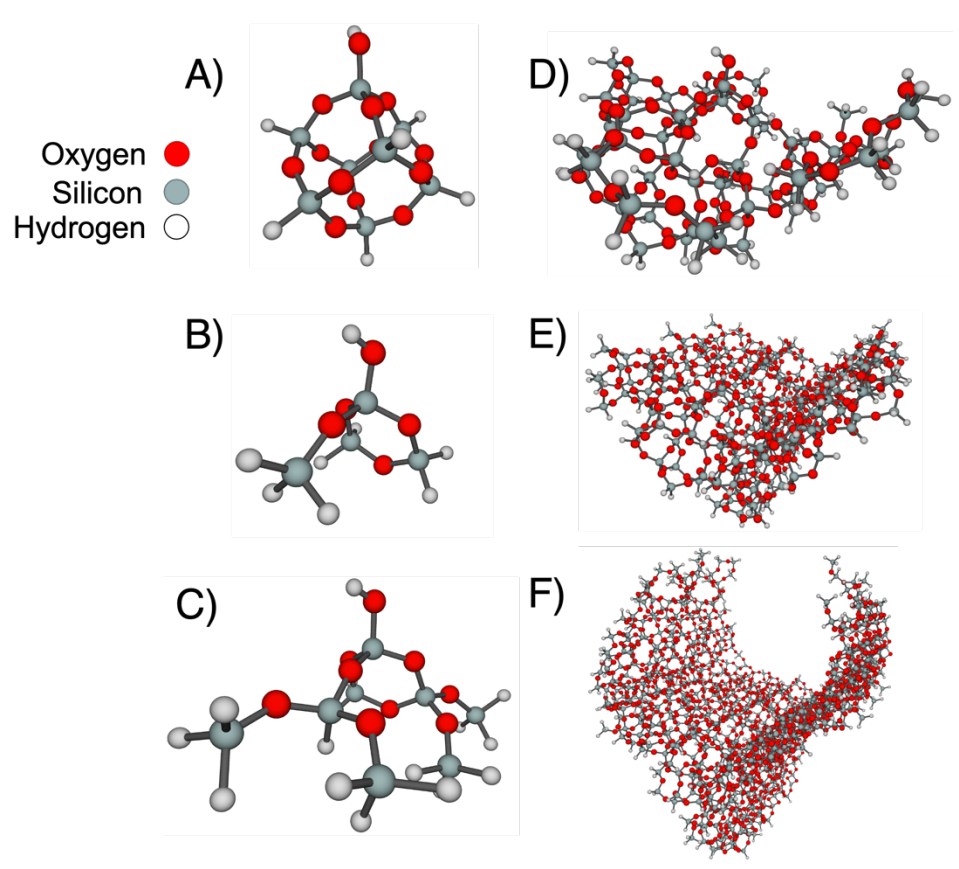


Figure 1: Representative images of =Si-OH models employed in this study. A) T8 silsesquioxane B) T4 sized model of the amorphous model generated by Tielens et al. C) T8 sized model of the amorphous model D) QM/MM model that uses the model in Figure 1C as the QM region and an MM region that terminates 11Å in radius from the central =Si-OH site. E) Same as Figure 1D but the MM region extends 20Å from the central =Si-OH site. F) Same as Figure 1D but the MM region extends 29Å from the central =Si-OH site

As mentioned in the previous section, models A-C are full QM calculations while D-F are QM/MM calculations that utilize model C as the QM region. Model D includes an MM region that extends 11 Å in radius from the central /≡Si-OH site, while Model E and F extend the region 20 Å and 29 Å in radius.

We also utilized seven amorphous silica geometries (adopted from Tielens et al.) in our study of ≡Ti-OH sites to examine the effect of distortion on enthalpies of adsorption.<sup>45</sup> ≡Ti-OH sites were generated by selecting seven isolated ≡Si-OH sites and replacing the Si atom with Ti followed by geometry optimization of the QM region (Figure 2). The local geometries of each ≡Ti-OH site (with an MM region extending 29Å in radius) examined in this study, along with the ≡Ti-OH T8 Silsesquioxane, are displayed in Table 1. Notably, the T8 Silsesquioxane shows a narrow distribution of Ti-O bond lengths compared to the amorphous models. Experimental characterization suggests that the average Ti-O bond lengths in Ti/SiO<sub>2</sub> materials lay between 1.80 Å and 1.81 Å and that the coordination of Ti atoms with O atoms is 4.<sup>28,31</sup> Thus, the average bond lengths of our models are all within 2% of the experimental value.

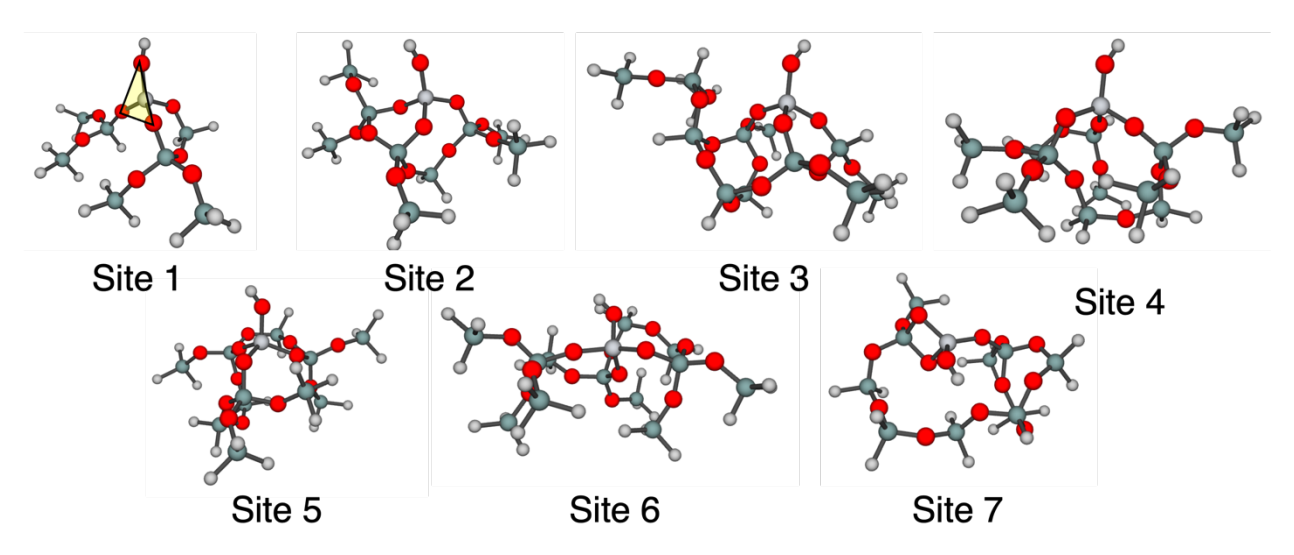


Figure 2: Illustrations of *=Ti-OH* sites (only the QM region is shown) generated by selecting seven isolated *=Si-OH* sites and replacing the Si atom with Ti followed by geometry optimization of the QM region. Large red spheres: oxygen, large dark grey spheres: silicon, large white spheres: titanium, small white spheres: hydrogen. An example of the "tetrahedral facet area" is highlighted on site 1.

Table 1: Bond lengths and tetrahedral facet areas of ≡Ti-OH sites\*

Table 1: bond lengths and tetrahedral facet areas of =11-OH sites								
Bond lengths (Å)								
Bond	Site 1	Site 2	Site 3	Site 4	Site 5	Site 6	Site 7	T8 silsesquioxane
Ti-OH	1.743	1.751	1.745	1.753	1.743	1.774	1.767	1.773
Ti-O1	1.779	1.786	1.795	1.773	1.792	1.801	1.816	1.780
Ti-O2	1.814	1.808	1.807	1.787	1.803	1.830	1.799	1.781
Ti-O3	1.832	1.816	1.814	1.797	1.891	1.816	1.835	1.781
Average	1.792	1.790	1.790	1.778	1.807	1.805	1.804	1.779
Tetrahedral facet areas (Ų)								
Facet	Site 1	Site 2	Site 3	Site 4	Site 5	Site 6	Site 7	T8 silsesquioxane
Facet 1	3.941	3.829	3.769	3.790	3.941	3.789	4.071	3.702
Facet 2	3.614	3.674	3.763	3.631	3.769	3.666	3.789	3.699
Facet 3	3.597	3.667	3.623	3.620	3.509	3.464	3.331	3.687
Facet 4	3.505	3.529	3.590	3.461	3.745	3.883	3.301	3.463
*** ** * * * * * * * * * * * * * * * * *								

<sup>\*</sup>Optimized at the  $\omega$ B97X-D/def2-SVP level of theory

# Results and Discussion

# Determination of $\Delta H_{ads}^o$ for polar adsorbates on $\equiv$ Si-OH groups

The value of  $\Delta H_{ads}^o$  for the interaction of polar adsorbates with the silanol groups on the surface of  ${\bf SiO}_{2\text{-}1023}$  were obtained by measuring the integrated absorbance for a characteristic IR band of the adsorbate as a function of adsorbate partial pressure and system temperature. The adsorption isotherms obtained this way were described by a Langmuir isotherm and analyzed accordingly. This procedure is illustrated below for the case of pyridine adsorption.

The Langmuir isotherm for pyridine adsorption as described as follows:

$$q_{ads} = q_{sat} \frac{K_{ads} P_{Py}}{(1 + K_{ads} P_{Py})} \tag{2}$$

Here  $q_{ads}$ ,  $q_{sat}$ ,  $K_{ads}$ , and  $P_{Py}$  refer to the quantity of adsorbed molecules of pyridine [mol Py], the amount of pyridine adsorbed at saturation [mol Py], the adsorption equilibrium constant, and the partial pressure of pyridine in the gas stream normalized by the standard pressure, 1 bar, respectively. A relationship between the amount of pyridine adsorbed and the integrated absorbance is derived from Beer's law. Thus,

$$q_{ads} = \frac{A_{py}S}{\epsilon} \tag{3}$$

where  $A_{py}$ , S, and  $\epsilon$  are the integrated absorbance [cm<sup>-1</sup>], the cross-sectional area of the pellet in the IR beam [cm<sup>2</sup>], and the integrated molar extinction coefficient [cm/mol Py], respectively. Substituting (3) into (2) gives:

$$\frac{A_{py}S}{\epsilon} = \frac{A_{max}S}{\epsilon} \frac{K_{ads}P_{Py}}{(1 + K_{ads}P_{Py})} \tag{4}$$

Both S and  $\epsilon$  appear on the left and right-hand sides of equation 4 and hence cancel out, resulting in equation (5).

$$A_{py} = A_{max} \frac{K_{ads} P_{Py}}{(1 + K_{ads} P_{Py})} \tag{5}$$

The equilibrium constant can be described in terms of  $\Delta H^o_{ads}$  and  $\Delta S^o_{ads}$ , the entropy of adsorption, both of which refer to the standard-state pressure of 1 bar and a standard coverage of 0.5 monolayers:

$$K_{ads} = \exp\left(-\frac{\Delta H_{ads}^o}{RT} + \frac{\Delta S_{ads}^o}{R}\right) \tag{6}$$

Selecting a standard state coverage of 0.5 monolayers ensures that configurational entropy is identically zero, and thus  $\Delta S_{ads}^o$  represents only molecular entropic changes. Thus, for a set of IR spectra measured at multiple temperatures and partial pressures of adsorbate, it is possible to fit  $A_{max}$ ,  $\Delta H_{ads}^o$ , and  $\Delta S_{ads}^o$  to the data. One can then normalize  $A_{max}$  by the integrated absorbance of the Si-O-Si overtone bands to allow for comparison between different silica samples.

#### Pyridine Adsorption on SiO<sub>2-1023</sub>

Figure 3A shows that the FTIR spectrum of pyridine adsorbed on  $SiO_{2-1023}$  exhibits two characteristic peaks at 1444 cm<sup>-1</sup> and 1594 cm<sup>-1</sup>. Both peaks correspond to ring-breathing vibrational modes (19b and 8a, respectively) for pyridine interaction with the hydrogen atom of  $\equiv$ Si-OH groups. For partial pressure and temperature changes the absorbance intensity of both peaks. A plot of the integrated absorbance vs. the partial pressure of pyridine is well-described by a Langmuir isotherm and is shown in Figure 3B. Values of  $A_{max}$ ,  $\Delta H_{ads}^o$ , and  $\Delta S_{ads}^o$  for both peaks obtained by fitting equations 4 and 5 to the data are presented in Table 2. We note that the values of these parameters are very similar for both features. This is to be expected because the peaks 19b and 8a have similar extinction coefficients. Find the value obtained for  $\Delta H_{ads}^o$  is -70 ± 1.8 kJ/mol and that for  $\Delta S_{ads}^o$  is -120 ± 3.2 J/mol·K.

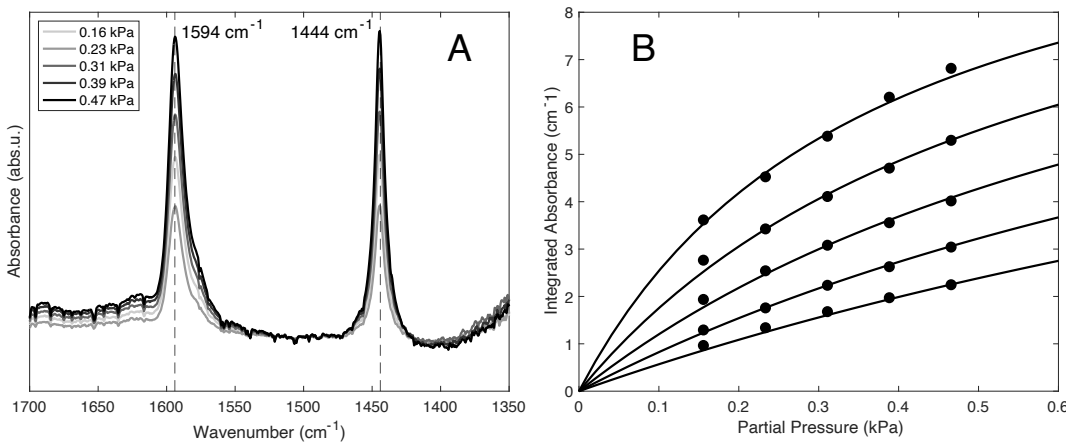


Figure 3: A) FTIR spectra (T = 460 K) and B) isotherms collected using peak centered at 1594 cm<sup>-1</sup> over the temperature range T = 420 K-460 K.

The next question to address is whether the value of  $\Delta H_{ads}^o$  determined corresponds to the interaction of pyridine solely with silanol groups rather than a combination of physisorbed (i.e. non-specific/liquid-like) pyridine and specifically adsorbed pyridine. An important indicator of the latter process is obtained by examining the effect of pyridine adsorption on the frequency of the  $\equiv$ SiO-H stretching vibration. As shown in Figure S5, in the absence of pyridine the SiO-H stretching vibration occurs at 3743 cm<sup>-1</sup> at 460 K. Upon adsorption of pyridine, the absorbance of this band decreases and a new, broad band centered at 3050 cm<sup>-1</sup> appears (Figure S6). The 700 cm<sup>-1</sup> redshift in the frequency of the  $\equiv$ SiO-H stretching vibration is a consequence of pyridine interacting with the  $\equiv$ SiO-H group. Figure S7 shows a near-perfect correlation between the integrated area of the perturbed  $\equiv$ SiO-H peak and the ring-breathing vibrational modes corresponding to pyridine itself, strongly suggesting that the value of  $\Delta H_{ads}^o$  determined from the isotherm presented in Figure 3B corresponds to adsorption of pyridine on silanol groups.

It is necessary, as well, to demonstrate that the measured value of  $\Delta H_{ads}^o$  corresponds to interactions specifically with isolated/geminal silanols, as opposed to vicinal silanols. We note in this connection that previous research has shown that polar molecules such as triethylamine and pyridine bind overwhelmingly to isolated/geminal silanols, and that vicinal silanols remain inert to these adsorbates.<sup>22,50</sup> To establish that this is the case in our work, we conducted a control experiment with our starting material  $SiO_{2-Hyd}$ .  $SiO_{2-Hyd}$  contains, approximately the same concentration of isolated silanols per gram as SiO<sub>2-1023</sub>30, but a higher concentration of H-bonded vicinal silanols (Figure S5). The isotherms for pyridine adsorption obtained by IR spectroscopy yielded a slightly higher value of  $\Delta H_{ads}^o$  ~-80 kJ/mol, and an identical saturation absorbance parameter (Figure S8 and Table S2). The identical saturation absorbance parameter confirms previously proposed arguments that pyridine binds exclusively to isolated/geminal silanols, whose densities do not change greatly under the thermal treatments used here. The effect of dehydroxylation on  $\Delta H_{ads}^o$  is small and similar to that determined by microcalorimetry for triethylamine adsorption on progressively dehydroxylated silica. 18 In that study, a decrease in the measured value of  $\Delta H_{ads}^o$  of ~10 kJ/mol was also observed for silica treated at higher temperatures. However, triethylamine coverages tracked with isolated/geminal silanol densities for all materials, indicating that the change in the enthalpies of adsorption results from subtle

modifications of isolated/geminal silanol sites through a currently unknown mechanism. These subtle modifications are evidenced by a small red-shift (~3 cm<sup>-1</sup>) in the isolated silanol SiO-H stretching frequency for the SiO<sub>2-Hyd</sub> vs. SiO<sub>2-1023</sub> bare materials (Figure S5).

Thus, the value of  $\Delta H^o_{ads}$  for pyridine measured here (~-70 kJ/mol) corresponds to the change in enthalpy of gas-phase pyridine to pyridine adsorbed to isolated/geminal silanols on the silica support at T = 420-460 K.

The enthalpies of adsorption of pyridine to  $SiO_2$ , as measured by calorimetry reported in the literature can vary. While our value agrees well with the dominant value measured from microcalorimetry by Kuznetsov et al. (~-72 kJ/mol)<sup>20</sup>, this value differs from measurements made by Dumesic and coworkers (-95 kJ/mol). The latter measurements were made at much lower coverages (< 0.1 Pyridine molecules/nm²). Kuznetsov et al. report similar initial enthalpies of adsorption (i.e. one data point at -93 kJ/mol), but the coverage over which this value persists (< 0.1 Pyridine molecules/nm²) is significantly lower than the estimated isolated/geminal silanol density of their materials (see Figure S9).<sup>20</sup> Conversely, they observe a relatively stable value (-72 kJ/mol) over a coverage range equal to the sum of the calculated isolated/geminal silanol density (~1.8 OH/nm²). Therefore, we propose that the site responsible for a  $\Delta H_{ads}^o$  of -95 kJ/mol observed at low coverages is distinct from an isolated/geminal silanol site and that the majority of isolated/geminal silanols adsorb pyridine with  $\Delta H_{ads}^o$  of -72 kJ/mol. However, we note that further investigations will be needed to unequivocally determine the physical origin of the highenergy site noted by other researchers.

## D<sub>3</sub>-Acetonitrile Adsorption on SiO<sub>2-1023</sub>

Figure 4A shows the IR spectra of  $d_3$ -acetonitrile adsorbed to  $SiO_{2-1023}$ . A well-defined peak is observed at 2272 cm<sup>-1</sup> corresponding to the C $\equiv$ N stretching frequency of  $d_3$ -acetonitrile interacting with  $\equiv$ Si-OH groups.  $^{20,51,52}$  We note that at the conditions shown in Figure 4, there is no evidence for a band at 2263 cm<sup>-1</sup> characteristic of non-specifically adsorbed (physisorbed)  $d_3$ -acetonitrile.  $^{51,52}$  An example of our peak fitting procedure is displayed in Figure S10.

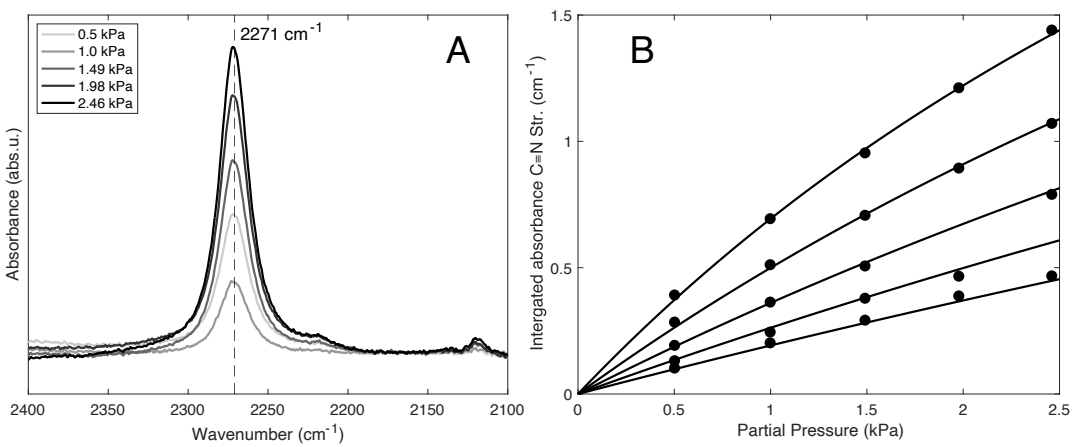


Figure 4: A)  $d_3$ -acetonitrile FTIR spectra (T = 460 K) and B) isotherms collected using peak centered at 2271 cm<sup>-1</sup> over the temperature range T = 420 K-460 K.

The value of  $\Delta H_{ads}^o$  derived from the isotherms shown in Figure 4B is -55 kJ/mol and is similar to that reported previously for d<sub>3</sub>-acetonitrile adsorbed onto silanol nests of zeolite beta (-55 kJ/mol)<sup>51</sup> and to the value for CH<sub>3</sub>CN adsorption measured by microcalorimetry for silica (-55.4 kJ/mol).<sup>20</sup> The value of  $\Delta S_{ads}^o$  for d<sub>3</sub>-acetonitrile adsorbed on silanol nests of zeolite beta is nearly 30% more negative than that measured in this work, suggesting that acetonitrile is more mobile on non-porous silica than when confined within a micropore of zeolite beta. As with pyridine, the integrated absorbance of the C $\equiv$ N stretching vibration is linearly proportional to the perturbed SiO-H stretch integrated absorbance (Figures S11 and S12), indicating the dominant phenomenon measured corresponds to acetonitrile interactions with silanols.

# Acetone Adsorption on SiO<sub>2-1023</sub>

Adsorption of acetone onto  $SiO_{2-1023}$  produces three detectable C=O stretching frequency bands at 1737 cm<sup>-1</sup>, 1712 cm<sup>-1</sup>, and 1699 cm<sup>-1</sup>, as seen in Figure 5A. We note that a small shoulder was always observed at 1737 cm<sup>-1</sup> in the absence of silica in our in-situ FTIR cell. This feature could be due to gas-phase acetone <sup>53</sup> or to a form of acetone interacting with the CaF<sub>2</sub> windows of the IR cell. This contribution was observed at all conditions and subtracted from the spectrum of acetone adsorbed on silica (Figure S13).

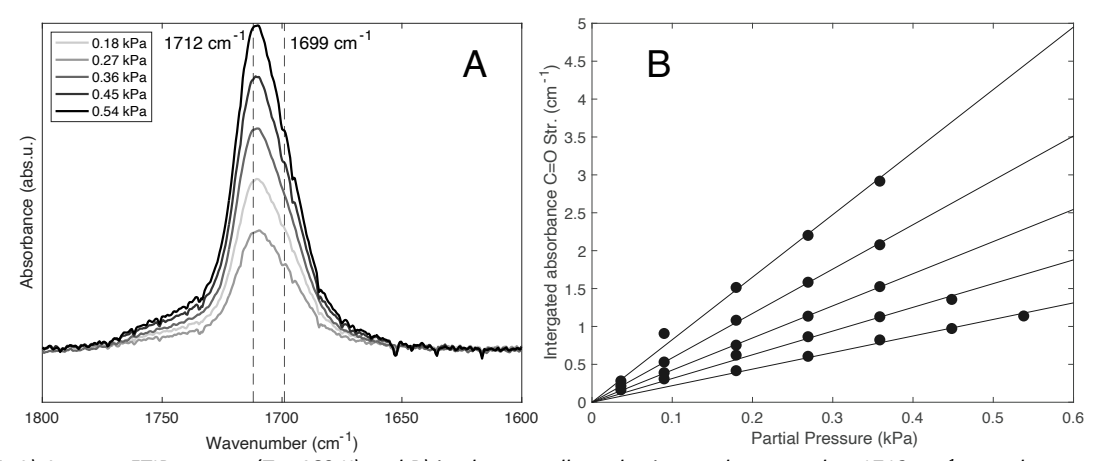
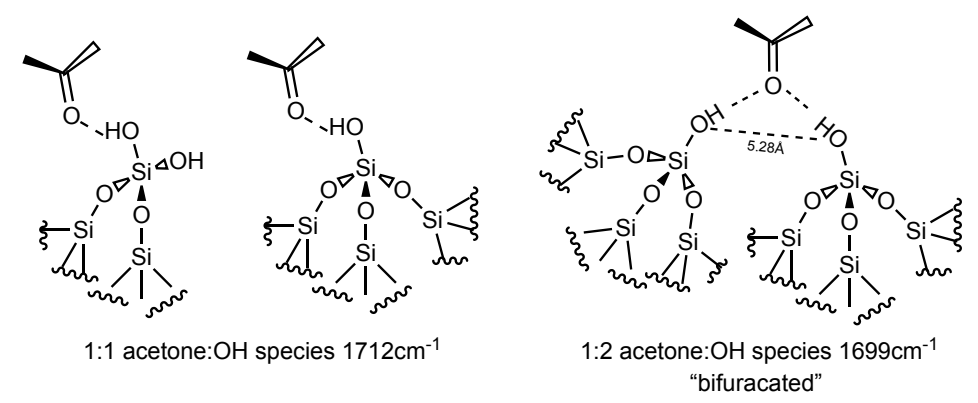


Figure 5: A) Acetone FTIR spectra (T = 460 K) and B) isotherms collected using peak centered at 1712 cm<sup>-1</sup> over the temperature range T = 420 K-460 K.

The band at 1712 cm<sup>-1</sup> is attributed to the C=O stretching frequency of acetone interacting with isolated or geminal silanol groups (Scheme 2),<sup>35</sup> whereas the band at 1699 cm<sup>-1</sup> is attributed to acetone to two proximate silanol groups (Scheme 1).<sup>35,54</sup> An example of our peak fitting procedure is displayed in Figure S14. Since the integrated absorbance for acetone adsorbed to isolated silanols (1712 cm<sup>-1</sup>) is within Henry's regime for the conditions investigated (Figure 5B), only the value of  $\Delta H_{ads}^o$  can be determined. The fitted values of  $\Delta H_{ads}^o$  for acetone adsorption on isolated and bifurcated silanols are -52 and -82 kJ/mol, respectively, which agree well with previous reports.<sup>35</sup> Once again, the integrated absorbance of the perturbed SiO-H stretching frequency is linearly proportional to the total adsorbed acetone, suggesting these  $\Delta H_{ads}^o$  are only describing silanol-acetone interactions (Figures S15 and S16).



Scheme 1: Adsorption configurations of acetone adsorbed to silanol groups on silica, as proposed in literature. <sup>35</sup> The optimal bond distance between bifurcated silanols is shown, as calculated by others. <sup>54</sup>

## Trimethylacetonitrile Adsorption on SiO<sub>2-1023</sub>

We also considered the adsorption of trimethylacetonitrile ((CH<sub>3</sub>)<sub>3</sub>CCN) adsorbed to  $SiO_{2-1023}$ . The IR spectrum for this adsorbate is presented in Figure 6A. The band appearing at 2243 cm<sup>-1</sup> is due to C=N stretching vibrations and is similar to that seen for adsorbed CD<sub>3</sub>CN. An example of our peak fitting procedure is displayed in Figure S17. The isotherms for trimethylacetonitrile are shown in Figure 6B. The value of  $\Delta H_{ads}^o$  determined from these isotherms is -64 kJ/mol, which is ~18% more exothermic than that determined for CD<sub>3</sub>CN on the same material (Table 2). This difference is consistent with the greater proton affinity of (CH<sub>3</sub>)<sub>3</sub>CCN compared to CD<sub>3</sub>CN.<sup>53</sup> This difference results from inductive effects of exchanging hydrogen (deuterium in the case of CD<sub>3</sub>CN) for electron-donating methyl groups. As with CD<sub>3</sub>CN, the peak area for the C=N stretching band is also linearly proportional to the perturbed SiO-H stretching frequency (Figures S18 and S19), indicating a silanol-adsorbate interaction.

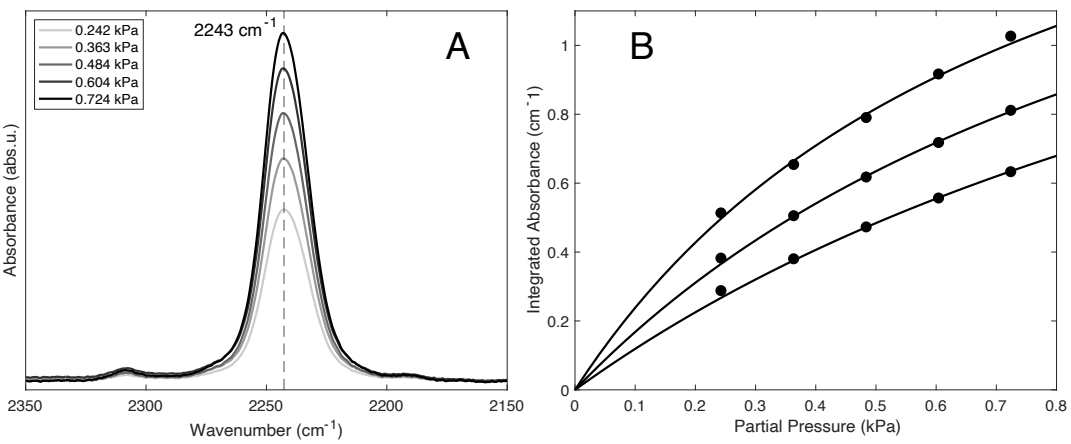


Figure 6: A) Trimethylacetonitrile FTIR spectra (T = 460 K) and B) isotherms collected using a peak centered at 2243 cm<sup>-1</sup> over the temperature range T = 440 K-460 K.

Table 2 compiles all peak centers used for coverage measurements, as well as fit parameters for  $\Delta H_{ads}^o$ ,  $\Delta S_{ads}^o$  (P° = 1 bar), and the normalized saturation parameter (Q<sub>sat</sub>).

Table 2: Assigned adsorption modes, peak centers, and Langmuir fitting parameters determined via FTIR coverage experiments for polar molecules adsorbed to  $SiO_{2-1023}$ 

Interaction	Adsorption Mode	Peak Center (cm <sup>-1</sup> )	$\Delta H^o_{ads}$ (kJ/mol)	$\Delta S^o_{ads}$ (J/mol K)	Normalized* Q <sub>sat</sub> x10 <sup>2</sup>
C₅H₅N−HO-Si≡	19b, ring-breathing	1444	-70 ± 1.8	-120 ± 3.2	5.68 ± 0.399
C₅H₅N−HO-Si≡	8a, ring-breathing	1594	-68 ± 1.5	-115 ± 2.8	8.08 ± 0.465
(CH <sub>3</sub> ) <sub>2</sub> C=O−HO-Si≡	C=O Str.	1712	-52 ± 1	N/M	N/M
$(CH_3)_2C=O-(HO-Si\equiv)_2$	C=O Str.	1699	-82 ± 1.9	-145 ± 3.3	2.36
CD₃CN–HO-Si≡	C≡N Str.	2272	-56 ± 1	-110 ± 1.5	3.83 ± 0.364
(CH <sub>3</sub> ) <sub>3</sub> CCN−HO-Si≡	C≡N Str.	2243	-64 ± 2	-104 ± 3.6	1.65 ± 0.108

<sup>\*</sup>unitless, normalized by the integrated absorbance of the Si-O-Si overtone region in the range 1735 cm $^{-1}$  – 2000 cm $^{-1}$ 

## Theoretical calculations for polar molecules adsorbed on isolated silanol groups

Having validated the determination of thermodynamic parameters from adsorption isotherms obtained from IR spectra, we wanted to assess the ability of our theoretical approach to estimate the enthalpies of adsorption of polar molecules onto silanol groups present on the surface of amorphous silica. To this end, we examined two models for representing the surface of silica. The first was a silsesquioxane structure comprising eight corner-sharing Si groups (Figure 1A). The second model is the structure shown in Figure 1F, which agrees well with experimental determinations of silanol densities, ring-size distributions, and Si-O-Si bond angles. Importantly, this model exhibits a silanol density of 1.7 OH/nm², which compares favorably with our measured value of 1.4 OH/nm² determined from TGA for SiO<sub>2-1023</sub>.

We found that an MM region terminating approximately 11 Å from the central silicon atom of an isolated silanol group was sufficiently large enough to capture nearly all contributions of the MM region to the predicted  $\Delta H_{ads}^o$  for pyridine (Figure S20). Interestingly, this also implies that the curvature of the model utilized for amorphous silica (see Figure 1F) has little impact on the  $\Delta H_{ads}^o$ . The difference in the  $\Delta H_{ads}^o$  of pyridine predicted using the site depicted in Figure 1B and Figure 1F is -32 kJ/mol, or, 41% of the  $\Delta H_{ads}^o$  predicted with the largest model. Recent full QM DFT calculations (with counter-poise basis set superposition error corrections) modeling the adsorption of  $H_2O_2$  and ethylene to silica-supported Nb metal sites found small differences (<10 kJ/mol) in predicted binding energies between large (12Å) and small (similar to Figure 1B) representations of the surrounding silica. <sup>55</sup> However, it is expected that  $H_2O_2$  and ethylene would be less affected by cluster size compared to pyridine, as they are smaller molecules and are subject to weaker pairwise-additive VDW interactions.

Based on these considerations, to avoid the possible influence of edge effects from the MM portion of the cluster, we utilized a cluster that extended 29 Å from the Si atom of the silanol group, since the computational cost of using a larger MM region was negligible.

We compared our predicted values of  $\Delta H_{ads}^o$  for triethylamine, ammonia, and tetrahydrofuran with those that we measured by IR spectroscopy and those reported in the literature determined by microcalorimetry. For ammonia, a detailed IR and calorimetric study revealed two dominant forms of ammonia adsorbed to SiO<sub>2</sub>. We utilized the value reported for ammonia adsorption onto isolated silanol groups (-58.4 kJ/mol).  $^{23}$ 

Figure 7 compares estimated values of  $\Delta H_{ads}^o$  to experimental values reported here and in the literature. It is immediately apparent that the T8 silsesquioxane model of amorphous silica underbinds all polar molecules in our dataset relative to experimental results. This finding is significant, considering that this model has been used extensively to calculate enthalpies of adsorption for various molecules interacting with silanol groups or  $\equiv$ M-OH (M = Ti, Zr, etc.) groups supported on silica.  $^{5,6,12-15,44}$  We note, however, that computational studies of microporous silicates have reported that small cluster models cannot capture the non-local interactions between the adsorbate and the surrounding support material, leading to enthalpy of adsorption predictions that are typically too small relative to experimental benchmarks.  $^{41}$  It should be clear

that these discrepancies are not the result of intrinsic DFT errors, which are expected to be relatively small ( $^{\sim}$  4 kJ/mol) for the non-covalent interactions studied here.<sup>39</sup>

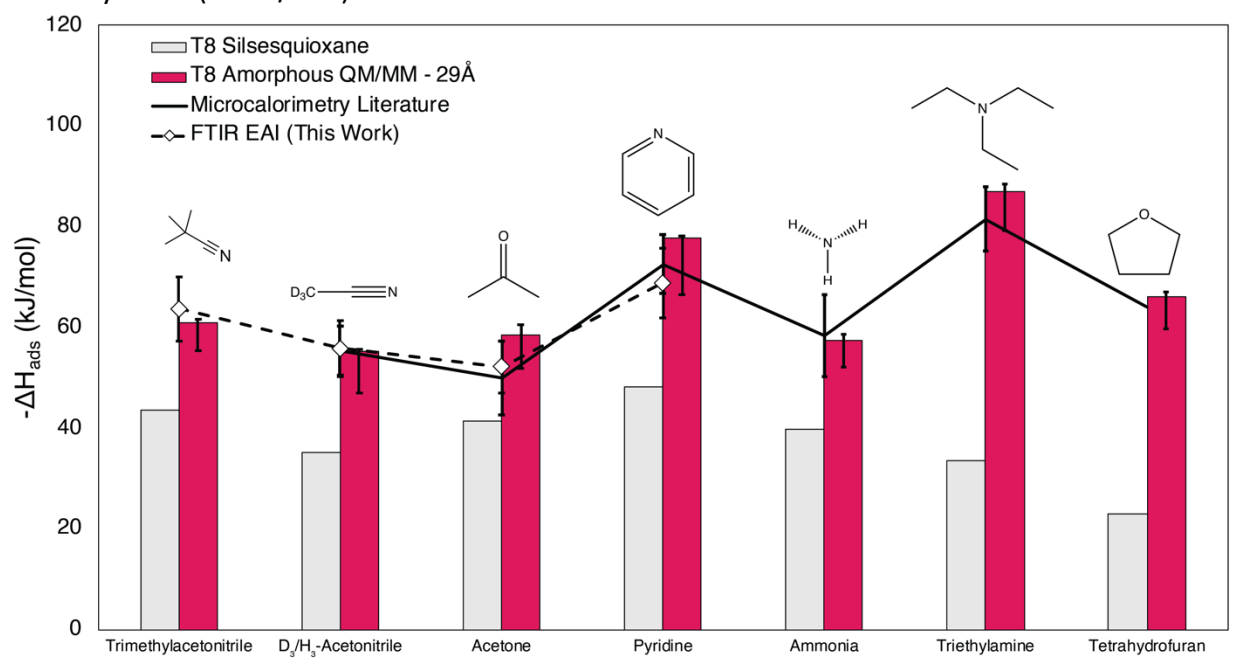


Figure 7: Comparison between experimental measurements (connected lines) and model predictions (bars). All calculations were performed for T = 460 K however similar conclusions are reached at other calculated temperatures. FTIR EAI = Fourier-transform Infrared Spectroscopy Equilibrium Adsorption Isotherm. Error bars on T8 amorphous QM/MM model show the spread of predicted  $\Delta H^o_{ads}$  made from multiple local minimum geometries, while the bar's value is the Boltzmann weighted  $\Delta H^o_{ads}$ . Error bars on all experiments are  $\pm 10\%$  of the  $\Delta H^o_{ads}$ .

A more detailed inspection of the isolated silanol in the amorphous model reveals that multiple adsorption geometries are plausible. In contrast to the T8 silsesquioxane, where the ≡Si-OH tetrahedron is symmetrical, the silanol tetrahedron on the amorphous model is distorted. Moreover, the model of amorphous silica used shows that the silica surface is irregular; therefore, one should not expect identical values of  $\Delta H_{ads}^o$  for locally optimized adsorption geometries sampled around the silanol. To address this complication, we optimized multiple geometries starting from initial guesses at each face (or side) of the HO-Si≡ tetrahedron. We discovered multiple minima (for each adsorbate) and found that each geometry exhibited a different value of  $\Delta H_{ads}^o$ . For instance, we located 5 optimized geometries for pyridine bound in an H-bonding configuration with the silanol that exhibited specific  $\Delta H_{ads}^o$  of -80.5, -78.1, -71.5, -66.5, and -66.8 kJ/mol. Using our thermal corrections to estimate the  $\Delta S_{ads}^o$  for each geometry allows us to assess their relative values of  $\Delta G_{ads}^o$ . Using these values of  $\Delta G_{ads}^o$ , we calculated the Boltzmann weight for each geometry, yielding 0.554, 0.255, 0.156, 0.03, and 0.002, respectively, for T = 460 K. This demonstrates that multiple pyridine geometries bound to the same silanol can contribute to the measured value of  $\Delta H_{ads}^o$ . This is consistent with NMR studies indicating that pyridine undergoes significant rotational motion on silica silanols, even at T = 174 K.56 Taking a Boltzmann average of the values of  $\Delta H_{ads}^o$  for different silanol geometries leads to  $\Delta H_{ads}^o$  = -77.9 kJ/mol, which agrees satisfactorily with experimental measurements.

The Boltzmann averaged  $\Delta H_{ads}^o$  for all adsorbates agree quantitatively with values determined experimentally from IR-based isotherms and measured microcalorimetrically. This agreement supports the model of amorphous silica and the computational protocol (QM/MM method) utilized. Considering that the parameters for the MM region were derived initially for microporous silicates (zeolites), the agreement between predicted and experimentally measured enthalpies of adsorption indicates the transferability of the parameters.  $^{41}$ 

The observed values of  $\Delta H_{ads}^o$  cannot be predicted reliably from a descriptor of the adsorbate basicity i.e., proton affinity, as seen in Figure S21, the correlation is weak and R²=0.79. This implies that a significant portion of the total  $\Delta H_{ads}^o$  arises from non-local interactions between the adsorbate and the surrounding silica, as mentioned previously. However, the degree of frequency redshift for the IR SiO-H stretch upon base complexation is more significantly correlated with proton affinity (Figure S22, R²=0.88). This suggests that this spectroscopic phenomenon represents local interactions between the adsorbing base and the silanol group, and that it should not be used as a sole indicator of the relative stability of adsorbed polar bases.

We also note that a more rigorous calculation of  $\Delta H_{ads}^o$  would require sampling all possible geometrical configurations for *all* silanol groups; however, this problem is currently intractable for a single silanol at the DFT level, let alone for all silanol groups present on the surface of amorphous silica. Thus, we will presume that the site used here is sufficiently representative of the surface of amorphous silica, as was noted by the authors of the model that we have used.<sup>45</sup> The agreement between experiments and our calculations, seen in Figure 7, supports this assumption.

## Entropies of adsorption ( $\Delta S_{ads}^{o}$ ) for SiO<sub>2</sub>

It is well-known that adsorbate entropies modeled using the rigid rotor - harmonic oscillator approximation (RRHO) can be inaccurate due to low-lying vibrational modes that should be modeled as hindered rotations or translations. To ur study employs a similar (and rougher) approach by representing low-frequency vibrational modes as free rotors. Unrethods are reliable in predicting gas-phase entropies; however, this quasi-RRHO (qRRHO) approach yields inaccurate predictions for  $\Delta S_{ads}^o$  as expected (Table 3). However, it is remarkable that Campbell and Sellers' empirical model for entropy loss upon adsorption (hereafter denoted as "Campbell") performs well, despite not being developed for adsorption on SiO<sub>2</sub>.

Briefly, the Campbell model is a simple linear correlation relating the gas phase and adsorbed phase entropy (equation 7).

$$S_{ads}^{o}(T) = S_{gas}^{o}(T) * 0.7 + 3.3R \tag{7}$$

where R is the ideal gas constant. This expression accurately predicts adsorbate entropies for nalkanes and small polar molecules adsorbing to metal oxides, metals, and carbon surfaces. Thus, adsorbates retain nearly two-thirds of their entropy in the gas phase, which is thought to be due to hindered translations and rotations of adsorbates across the surfaces of these materials.<sup>57</sup> However, other studies have reported its accuracy in predicting the entropies of ethanol and

water adsorbed to monomeric framework Sn sites in microporous silicates ("Sn-BEA zeolites").<sup>58</sup> The predictions by equation 7 agreed with ab initio molecular dynamics (AIMD) simulations which showed that ethanol and water retain significant localized translations around the Sn site. Therefore, the accuracy of equation 7 with experimental data should not be interpreted as a deep understanding of the adsorption phenomena in question. Nevertheless, it does suggest significant adsorbate motion relative to the assumptions of the RRHO model.

The discrepancy for trimethylacetonitrile could be expected since the correlation did not include molecules with tert-butyl groups. Developing methods for accurate predictions of  $\Delta S_{ads}^o$  is an active area of research and lies outside the scope of this work, which is focused on  $\Delta H_{ads}^o$ ; however, we note that simplified methods are needed for accurate prediction of both parameters using DFT potential energy surfaces, and a small number of DFT calculations. For now, we recommend a combination of QM/MM modeling for  $\Delta H_{ads}^o$  combined with empirical estimates for  $\Delta S_{ads}^o$  when accurate  $\Delta G_{ads}^o$  estimates are desired.

Table 3: Gas phase entropies and entropies of adsorption,  $P^o = 1$  bar – comparison between predictions and experiments

Molecule	S <sub>gas,expt</sub> (T=298 K)	S <sub>gas,qRRHO</sub> (T=298 K)	S <sub>gas,qRRHO</sub> (T=460 K)	ΔS <sub>ads,qRRHO</sub> (T=460 K)*	ΔS <sub>ads,Campell</sub> (T=460 K)** <sup>57</sup>	$\Delta S_{ads,expt}$
Pyridine	282.8 <sup>59</sup>	281.1	322.2	-186.7	-124.1 ± 18	-120 ± 3.2
d3-acetonitrile	N/A	250.6	279.1	-149.6	-111.2 ± 18	-110 ± 1.5
h3-acetonitrile	245.5 <sup>60</sup>	242.7	267.9	N/A	-107.8 ± 18	N/A
Acetone	295.5 <sup>35</sup>	298.0	335.6	-185.0	-128.1 ± 18	-122 <sup>35</sup>
Trimethylacetonitrile	333.2 <sup>61</sup>	329.4	389.5	-180.6	-144.3 ± 18	-104 ± 3.6

<sup>\*</sup>Boltzmann average of multiple equilibrium geometries; \*\*uses  $S_{gas,qRRHO}$  to compute adsorbed phase entropy, then takes the difference to calculate  $\Delta S_{ads,Campell}$ . Error bars represent one standard error reported in ref <sup>57</sup>

## Characterization of Ti/SiO<sub>2,1023</sub>

DRUV/Vis spectra were acquired to determine the coordination of Ti in  $Ti/SiO_{2,1023}$ . The UV/Vis spectrum for  $Ti/SiO_{2,1023}$ , shown in Figure 8A, displays a sharp peak centered at 225 nm, consistent with ligand-to-metal charge transfer (LMCT) transitions of isolated, tetrahedral  $\equiv$ Ti-OH centers. This spectrum was used to construct a direct-transition Tauc plot, from which the band-edge energy was calculated. As noted in Table 4, the band-edge energy for  $Ti/SiO_2$  is 4.75eV, which agrees very well with the values previously reported for  $Ti/SiO_2$  prepared with very low loadings of  $Ti.^{31,36,37}$ 

The Ti K-edge XAS spectrum displays a pre-edge feature centered between 4969.8 eV and 4970.1 eV. This feature arises from 1s→3d electronic transitions that become dipole-allowed due to 3d/4p mixing when the Ti and its ligands are in a tetrahedral geometry. At ambient temperature (300 K), pre-exposure of Ti/SiO<sub>2,1023</sub> to water vapor results in the coordination of water to Ti, breaking the Ti tetrahedral symmetry and producing a pre-edge feature that is weak in intensity relative to the tetrahedral standard, Ti[OSiPh₃]₄, and centered at 4970.1eV (Figure 8B). Increasing the temperature under flowing helium drives off the water, reestablishing the tetrahedral geometry, and blue-shifting the peak by 0.3 eV to 4969.8eV and increasing its intensity 2-fold. The pre-edge intensity rises rapidly with the initial increase in temperature but changes less as the temperature reaches 673 K, indicating complete desorption of coordinated water, consistent with other studies for this material. The pre-edge feature does not change significantly after lowering the temperature to 553 K following water desorption, indicating a weak thermal effect on peak intensity (Figure S23).

Previous studies on Ti/SiO<sub>2</sub> synthesized using similar techniques have reported lower pre-edge intensities than those found here. 64 However, it is important to note that these materials were vacuum treated only to 423 K, which is not sufficiently high to remove all coordinated water.<sup>28</sup> The normalized pre-edge peak intensity for Ti/SiO<sub>2,1023</sub> is 17% lower than Ti[OSiPh<sub>3</sub>]<sub>4</sub>, even after desorption of coordinated water. It has been suggested that a lower intensity pre-edge peak for Ti/SiO<sub>2</sub> could be due to a linear combination of hexacoordinated and tetrahedral Ti metal centers<sup>65</sup>; however, our UV/Vis results are inconsistent with this interpretation since there is no detectable presence of hexacoordinated species, which would be characterized by peaks >300nm.<sup>62</sup> An alternative explanation is suggested by recent DFT calculations. Tetrahedral distortion was found to significantly decrease the intensity of the pre-edge XANES feature predicted by Time-Dependent DFT for isolated V(V)/SiO<sub>2</sub> species.<sup>13</sup> A similar effect would be expected for Ti(IV) cations, as both V(5+) and Ti(IV) cations have identical electronic configurations. Moreover, the same electronic transition is being probed (1s $\rightarrow$ 3d/4p transition) for both cations. Thus, at the extremes, two hypotheses about the structure of monomeric ≡Ti-OH in Ti/SiO<sub>2,1023</sub> can be postulated from these findings. 1) The sample consists of many tetrahedral ≡Ti-OH sites that exhibit specific pre-edge intensities consistent with Ti[OSiPh₃]4 and a small fraction of tetrahedrally distorted ≡Ti-OH structures exhibiting weak pre-edge features. This hypothesis is similar to that proposed for Cr/SiO<sub>2</sub>.66 2) All ≡Ti-OH sites are similarly distorted and produce a weaker pre-edge feature relative to Ti[OSiPh<sub>3</sub>]<sub>4</sub>. Ti K-edge XAS cannot discriminate between these two possibilities, since it is a bulk technique; however, the degree to which  ${\sf Ti/SiO_{2,1023}}$  can be interrogated will be discussed below by measuring the  $\Delta H_{ads}^o$  of pyridine adsorption as a function of pyridine loading.

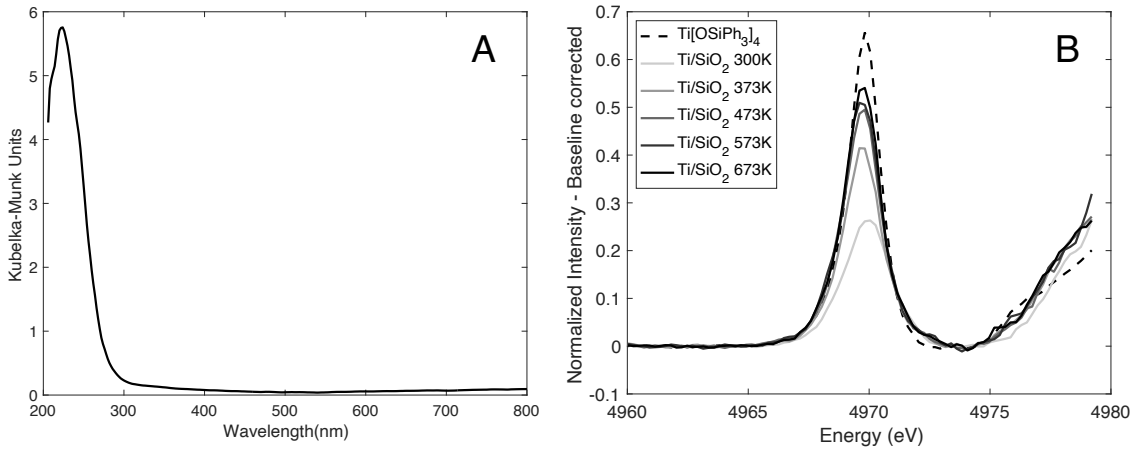


Figure 8: A) Diffuse-reflectance UV/Vis spectrum of **Ti/SiO**<sub>2-1023</sub> at 553.15 K under flowing He and B) pre-edge XANES spectra of **Ti/SiO**<sub>2-1023</sub> and **Ti[OSiPh<sub>3</sub>]<sub>4</sub>**. The pre-edge XANES spectra for **Ti/SiO**<sub>2-1023</sub> was taken under flowing He.

Table 4: ICP characterization, UV Vis edge energies

Table 4. for characterization, of the cage energies					
Material	LMCT Edge(eV)/ Peak(nm)	Ti/nm²	Method	Ref	
Ti/MCM-41	4.7	0.07	IWI*	67	
Ti/SiO <sub>2</sub>	4.66/210	0.24	IWI*	68	
Ti/SBA15	N.M./225	0.61	Ti(OiPr)[Osi(OiBu)₃]₃ – graft	25	
Ti/SiO <sub>2</sub>	4.53/225	0.24	Calix[4]arene-Ti <sup>IV</sup> graft	28	
Ti/SiO <sub>2,1023</sub>	4.75/224	0.084	Cp – graft	This Work	
Ti/SiO <sub>2,1023</sub> (sample 2)	4.84/224	0.089	Cp – graft	This Work	

<sup>\*</sup>Incipient wetness impregnation

## Pyridine adsorption on Ti/SiO<sub>2,1023</sub> – experiments and theory

An adsorbate that does not react and consume  $\equiv$ Ti-OH sites is required to measure equilibrium adsorption isotherms. Unfortunately, we observed decomposition and consumption of  $\equiv$ Ti-OH sites over time for all of the adsorbates we tested for SiO<sub>2</sub> except pyridine. Thus, we restrict our analysis for **Ti/SiO**<sub>2,1023</sub> to pyridine.

The IR spectra of pyridine adsorbed to **Ti/SiO<sub>2,1023</sub>** were collected at temperatures of 503.15 K to 623.15 K and partial pressures between 0.035 and 0.49 kPa. Figure 9A shows the spectrum of adsorbed pyridine acquired at 503.15 K in the presence of 0.42 kPa pyridine. Peaks are observed at 1605 cm<sup>-1</sup>, 1489 cm<sup>-1</sup>, and 1447 cm<sup>-1</sup>. These features correspond to ring-breathing vibrational modes of pyridine interacting directly with a Lewis acid center.<sup>10</sup> No absorbance is observed between 1540-1550 cm<sup>-1</sup>, indicating the absence of pyridinium ions which would be formed by pyridine adsorption at Brønsted acid sites.<sup>10</sup> We also note that the band at 1605 cm<sup>-1</sup> is redshifted relative to that observed for pyridine adsorbed on P25 TiO<sub>2</sub> at 470 K (1609 cm<sup>-1</sup>)<sup>69</sup>, suggesting the absence of TiO<sub>2</sub>, which is consistent with our UV/Vis observations (see Figure 8). The peak center is within a 2 cm<sup>-1</sup> range for all conditions examined.

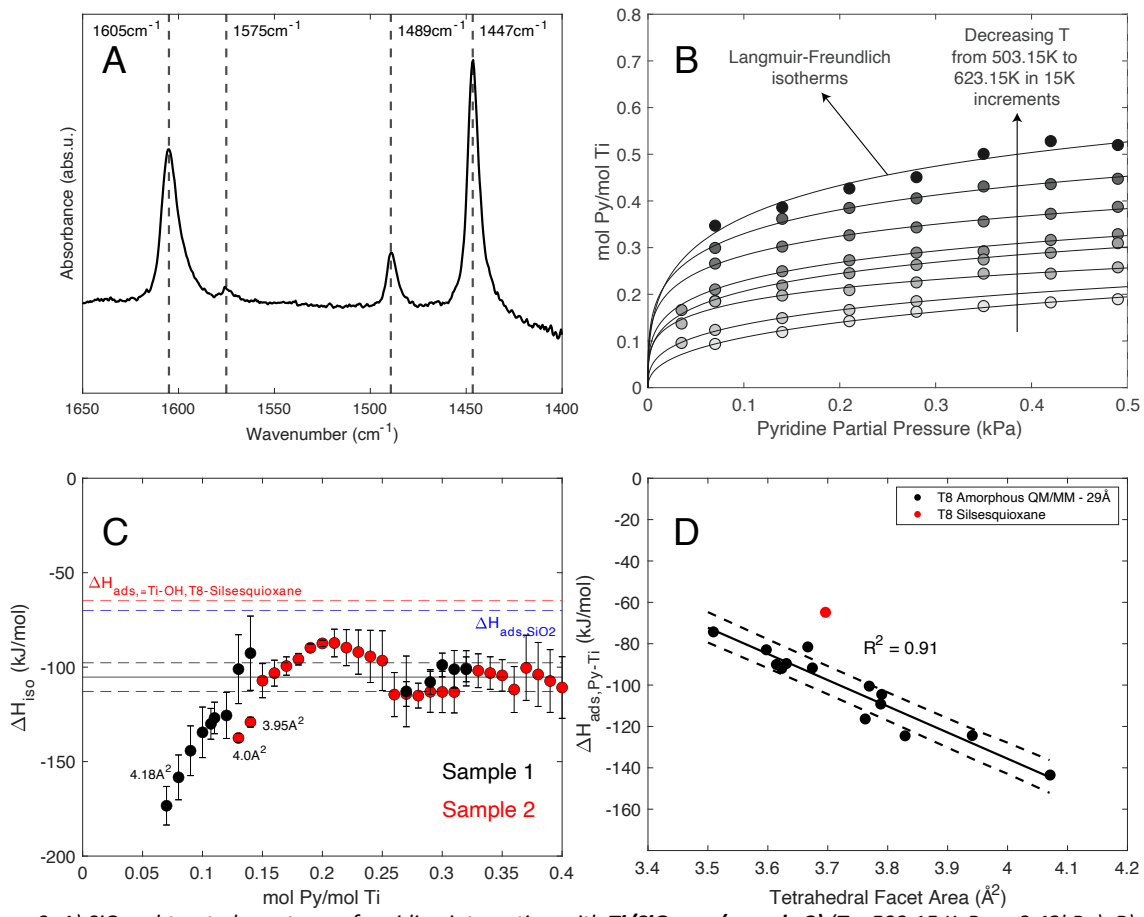


Figure 9: A)  $SiO_2$  subtracted spectrum of pyridine interacting with **Ti/SiO**<sub>2,1023</sub> (sample 2) (T = 503.15 K,  $P_{py} = 0.42$ kPa). B) pyridine coverage on **Ti/SiO**<sub>2,1023</sub> (sample 2) (mol Py/mol Ti) as a function of partial pressure (kPa). Langmuir-Freundlich isotherm fits are shown as lines. Covers T-range 503.15 K through 623.15 K except 593.15 K. C) Isosteric enthalpy of adsorption of pyridine to  $\equiv$ Ti-OH sites as a function of pyridine coverage (mol Py/ mol Ti). Facet areas calculated from the correlation presented in Figure 9D are labeled. The dashed blue line shows the experimental  $\Delta H_{ads}^o$  of pyridine to isolated/geminal silanols.

The solid black line shows the predicted  $\Delta H^o_{ads}$  of pyridine to a  $\equiv$ Ti-OH site with a facet area derived from EXAFS (3.76Ų), while dashed black lines are one standard error of the  $\Delta H^o_{ads}$  prediction from the correlation in Figure 9D. D) QM/MM  $\Delta H^o_{ads}$  calculations (T = 598 K) as a function of the tetrahedral facet area of the  $\equiv$ Ti-OH site to which pyridine is bound (an example of the area in question is highlighted on the molecular geometry within the figure). The solid line is the linear fit, while the dashed lines are one standard error of the y-estimate ( $\Delta H^o_{ads}$ ).

To analyze pyridine features associated exclusively with adsorption to ≡Ti-OH sites, we subtracted the spectrum of pyridine bound to  $SiO_{2,1023}$  at each condition using the same mass of powder (±1 mg) to form the pellet. To ensure the accurate removal of features during the subtraction process, we conducted a control experiment to subtract the spectra from two consecutive  $SiO_{2,1023}$  (Figures S24, S25, and S26) runs. The subtracted peak areas equal zero, indicating that this procedure properly removes contributions associated with pyridine bound to silanol groups and confirms that our pellet preparation method is reproducible.

Having established this subtraction procedure, we repeated the analysis to remove the overlapping features of pyridine interacting with  $SiO_{2,1023}$  from the spectrum of  $Ti/SiO_{2,1023}$  acquired for all experimental conditions. After subtraction, we observed a new feature at 1575 cm<sup>-1</sup>, attributed to ring-breathing mode 19a, which can be observed when pyridine interacts molecularly with a Lewis acid center.<sup>10</sup> The appearance of this mode after  $SiO_2$  subtraction further lends credence to our subtraction protocol. Moreover, no significant distortion or oversubtraction artefacts were observed in all  $SiO_{2,1023}$  subtracted spectra (Figure 9A). Thus, the experimental protocol we have developed monitors the surface coverage of pyridine bound exclusively to  $\equiv Ti$ -OH sites.

To calculate the fractional coverage (mol pyridine/mol Ti), we applied the appropriate extinction coefficient for the peak centered at 1605 cm $^{-1}$ . We did not analyze the feature at 1447 cm $^{-1}$  because IR absorption from the CaF $_2$  optical windows of our in-situ cell began to interfere with this peak above 593 K. The temperature range of this experiment was broad compared with our experiment with  $SiO_{2,1023}$  alone; therefore, we also accounted for the temperature dependence of the extinction coefficient using the following expression: $^{71}$ 

$$\epsilon(T) = \epsilon_{1605cm^{-1}}(T = 423K) - 0.001 * (T - 423K)$$
(8)

where  $\epsilon_{1605cm^{-1}}(T=423~K)$  is equal to 0.9733 cm/µmol pyridine<sup>70</sup> and T is the temperature of the experiment in Kelvin. We note that extinction coefficients for pyridine adsorbed to Lewis acid metal supported silicates fall in the range of 0.7-1.5 cm/µmol.<sup>49</sup> We also note that our experimental setup, i.e., the brand of spectrometer, detector type, pellet size and mass were similar to those used for the experiment reported in the ref.<sup>70</sup> This further supports the applicability of the extinction coefficients reported by the authors of this work to our experiments.

The adsorption Isotherms for  $Ti/SiO_{2,1023}$  are shown in Figure 9B. In contrast to what was observed for pyridine adsorption to the silanol groups present on  $SiO_{2,1023}$ , the data for pyridine adsorption on  $Ti/SiO_{2,1023}$  cannot be described by a Langmuir isotherm, for which  $\Delta H_{ads}^o$  is assumed to be constant. (Figure S27). Therefore, we calculated the isosteric enthalpies of

adsorption ( $\Delta H^o_{iso}(\theta)$ ) as a function of pyridine coverage. To do so, we fitted the experimental data points shown in Figure 9B to a Langmuir-Freundlich isotherm (equation 9) and used this expression to estimate coverages between experimental data points.

$$Q = Q_o \frac{(KP)^n}{1 + (KP)^n} \tag{9}$$

Values of Q<sub>o</sub>, K, and n were fitted to each isotherm (Figure 9B). We then estimated the partial pressure necessary to achieve a given mol Py/mol Ti to determine the isosteres, which were then used together with the Clausius-Clapeyron equation (equation 10) to calculate the isosteric enthalpy of adsorption.

$$\Delta H_{iso}(\theta) \left[ \frac{kj}{mol} \right] = \left( \frac{dln(P_{pyridine}[bar])}{d\left(\frac{1}{RT}\right)} \right)_{\Theta}$$
 (10)

In carrying out this procedure, at least three data points were taken per isostere, and we only extrapolated an isotherm within 10% of the minimum/maximum coverage. This point is necessary since values of  $\Delta H^o_{iso}(\theta)$  can be sensitive to extrapolation percentages (Figures S28 and S29) even though general trends are preserved. Thus, extrapolation by more than 10% should be avoided so that values of  $\Delta H^o_{iso}(\theta)$  do not include these artefacts.

Figure 9C shows that for coverages less than 15%, the magnitude of  $\Delta H_{iso}^{o}(\theta)$  decreases with increasing coverage, and then becomes relatively constant for coverages above 15%. We found similar behavior for two different batches of Ti/SiO<sub>2-1023</sub> (see Figure S30 for Langmuir-Freundlich fitting for **Ti/SiO<sub>2,1023</sub> (sample 1)** used to calculate  $\Delta H_{iso}^{o}(\theta)$  for sample 1 in Figure 9C, and Figure S31 for UV/Vis characterization of sample 2, the edge energy of which is presented in Table 4). To assess the possibility that distortion of tetrahedral ≡Ti-OH sites could explain the adsorption enthalpy variation observed at low pyridine coverages in our experiments, we calculated the  $\Delta H_{ads}^{o}$  for a series of representative  $\equiv$ Ti-OH sites. Each of these sites was defined by replacing an ≡Si-OH group on the surface of our model of amorphous silica with a ≡Ti-OH group and then optimizing the resulting structure. Figure 2 illustrates the geometry of each ≡Ti-OH group obtained in this manner and the areas of the three triangular facets for each group. We note that the triangular facets of each ≡Ti-OH group exhibit different surface areas, and that the set of areas is different for the seven ≡Ti-OH groups chosen as representatives. To pursue our objective, we calculated the enthalpies of pyridine adsorption on each facet for each of the seven ≡Ti-OH groups. The results, presented in Figure 9D, show that the value  $\Delta H_{ads}^o$  correlates well (R<sup>2</sup> = 0.91) with the area of the triangular facet; as the facet area increases, the predicted value of  $\Delta H_{ads}^o$ decreases monotonically. We were unable to acquire data for all facet areas since some facets were inaccessible to pyridine due to steric interference by the surrounding silica. What we find is that as the area of the facet increases from 3.5  $\text{Å}^2$  to 4.07  $\text{Å}^2$ , the values of  $\Delta H_{ads}^o$  decrease from -74 kJ/mol to -145 kJ/mol, respectively. This descriptor is reminiscent of the "accessible coordination pocket" that others have correlated with ethylene epoxidation activation energies with Nb/SiO<sub>2</sub> catalysts.<sup>55</sup>

As noted in our discussion of the physical characteristics of  $\equiv$ Ti-OH groups, EXAFS characterization suggests that the average Ti-O bond length is between 1.80 Å and 1.81 Å and that the coordination of Ti atoms with O atoms is  $4.^{28,31}$  Assuming this geometry is tetrahedral, which is supported by the intense pre-edge XANES features, leads to the conclusion that the triangular facet area ranges from 3.74 Ų to 3.78 Ų; therefore, we take 3.76 Ų as the EXAFS determined Ti facet area. For this facet area the correlation presented in Figure 9D gives a value of  $\Delta H_{ads}^o = -105\pm10$  kJ/mol, which agrees remarkably well with the average experimentally determined value of  $\Delta H_{ads}^o = -104\pm10$  kJ/mol observed in Figure 9C for pyridine coverages greater than 15% (Figure 9C). At lower coverages, larger tetrahedral facet areas are necessary to achieve agreement between our calculations and experiments. Therefore, we propose that tetrahedral distortion of  $\equiv$ Ti-OH sites can explain lower values  $\Delta H_{ads}^o$  determined for coverages <15%. We note this proportion of distorted sites is similar to that reported for isolated sites of Cr, W, and Mo supported on silica. 11,66,72

We also wish to stress that our ability to interpret the isosteric enthalpies of adsorption of pyridine is a consequence of the model for  $\equiv$ Ti-OH sites on **Ti/SiO**<sub>2,1023</sub> that we have used. As indicated by the red point in Figure 9C and red dashed line in Figure 9D, calculations of  $\Delta H_{ads}^o$  determined using the T8 silsesquioxane representation of  $\equiv$ Ti-OH groups under predicts the value of this parameter relative to its experimentally determined value, as seen for **SiO**<sub>2,1023</sub>, further indicating the insufficiency of the size of this model.

We conclude that only a small fraction (~15%) of ≡Ti-OH sites are distorted tetrahedral structures, while the rest are relatively symmetrical and consistent with the geometries measured by EXAFS. We further propose that the observed pre-edge XANES intensity reduction relative to our tetrahedral standard results from a linear combination of distorted (weak pre-edge feature¹³) and symmetric ≡Ti-OH structures (strong pre-edge feature).

The magnitudes of  $\Delta H_{ads}^o$  measured here for  $\equiv$ Ti-OH sites strongly disagree with previous researchers.  $^{26,27}$  Unfortunately, the methods of data acquisition and analysis employed by others were, in our opinion, inadequate. Firstly, the IR peaks used for coverage estimates of pyridine to the  $\equiv$ Ti-OH sites overlap significantly with peaks associated with pyridine adsorption to  $\equiv$ Si-OH groups of SiO<sub>2</sub> and no attempt was made to remove these features. Secondly, the analysis employed (Van't Hoff analysis of isobars) is only accurate in the limit of zero coverage for a theoretical Langmuir isotherm, a form which many adsorption phenomena follow. As a result, the reported values of  $\Delta H_{ads}^o$  were between -10 and -30 kJ/mol, which are far lower than the enthalpies of liquefaction of pyridine ( $\Delta H_{liq}^o$  = -40.3 kJ/mol) and the value of  $\Delta H_{ads}^o$  for pyridine adsorption on the SiO<sub>2</sub> support (-70 kJ/mol). Significant underestimation of  $\Delta H_{ads}^o$  and, at worst, reversed trends in  $\Delta H_{ads}^o$  across materials are expected from V'ant Hoff isobar analysis (See SI section 27 for full discussion).

# Energy decomposition analysis to understand the physical origin of the effects of site distortion on $\Delta H_{ads}^o$

To further understand the physical phenomenon governing the change in  $\Delta H_{ads}^o$  with site distortion, we performed energy decomposition analysis (EDA) calculations using methods developed by Horn et al.<sup>29</sup> For this analysis, we only examined the components of the electronic energy of adsorption ( $\Delta E_{ads}^o$ ), as this is the largest component of the  $\Delta H_{ads}^o$ .

The EDA unravels the  $\Delta E^o_{ads}$  into five components. The overall binding energy is calculated as:

$$\Delta E_{ads}^{o} = \Delta E_{GD,Ti} + \Delta E_{GD,Py} + \Delta E_{FRZ} + \Delta E_{POL} + \Delta E_{CT}$$
 (11)

where  $\Delta E_{GD,x}$  captures the geometric distortion penalty of x (the  $\equiv$ Ti-OH site or the pyridine molecule), or the energy difference between x in the complex geometry and its optimal geometry in vacuum;  $\Delta E_{FRZ}$  is the interaction energy resulting from permanent electrostatic charges, Pauli-repulsion, and dispersion interactions (we include the MM VDW interaction in this term);  $\Delta E_{POL}$  is the energy lowering due to polarization of the orbitals on each fragment in the presence of the other fragment; and  $\Delta E_{CT}$  accounts for the energy lowering due to inter-fragment charge transfer (electron delocalization) between the  $\equiv$ Ti-OH site and the pyridine molecule.

Interestingly, only two components of the EDA change appreciably with the facet area,  $\Delta E_{FRZ}$  and  $\Delta E_{GD,Ti}$  (Figure 10). We fit linear models for each component to understand the trends quantitatively (Table 5). Taking the slope as the first derivative of the component in question with respect to tetrahedral facet area suggests that the geometric distortion penalty of the  $\equiv$ Ti-OH site is most strongly correlated to the  $\Delta E_{ads}^{o}$  (slope is 60% of the slope for  $\Delta E_{ads}^{o}$ ). We can take the x-intercept as the tetrahedral facet area where  $\Delta E_{GD,Ti}$  is zero, which yields 4.35 Ų.  $\Delta E_{GD,Ti}$  must be positive semi-definite²9, therefore this facet area also corresponds to the upper bound of the magnitude of  $\Delta E_{ads}^{o}$ , which we estimate to be -172.5 kJ/mol based on our linear correlation. Assuming this facet area arises from a  $\equiv$ Ti-OH site in perfect tetrahedral geometry implies Ti-O bond lengths of 1.94 Å, or nearly 0.14 Å longer than values derived from EXAFS. All attempts to locate a  $\equiv$ Ti-OH site with this size facet area were unsuccessful using the amorphous silica model we employed, but sites with this level of distortion are likely to be extremely uncommon. This marks the first utilization of EDA as a means of estimating the maximum  $\Delta E_{ads}^{o}$  of an adsorbate to a SSMC.

 $\Delta E_{FRZ}$  has the second largest facet area dependence (~30%), and the relationship displays more scatter around our linear fit relative to  $\Delta E_{GD,Ti}$  (see Figure 10). All other components display minimal scatter around their associated linear fits, indicating that the variability in the  $\Delta E_{ads}^{o}$  with respect to facet area arises primarily from variation in  $\Delta E_{FRZ}$ . The variability in  $\Delta E_{FRZ}$  with facet area is expected since  $\Delta E_{FRZ}$  includes the interaction of pyridine with the MM region of the surrounding silica support which will vary considerably for each  $\equiv$ Ti-OH site in an amorphous lattice regardless of its local geometry. We note one outlier for  $\Delta E_{GD,Ti}$  with a facet area of 3.66Ų (site 2, face 3 in Table 1) exhibits a larger  $\Delta E_{GD,Ti}$  relative to the linear fit because of a siloxane bridge located directly in front of the facet (can be seen in Figure 2, site 2). The final geometry of the  $\equiv$ Ti-OH site after pyridine adsorption is more significantly distorted than would be expected

since pyridine is avoiding the steric repulsion with this siloxane bridge, leading to a more positive  $\Delta E_{GD,Ti}$  than predicted by the linear fit.

Surprisingly,  $\Delta E_{POL}$  and  $\Delta E_{CT}$  remain nearly constant for all facet areas. This discovery challenges previously held conjectures regarding silica-supported Zr, W, and Nb sites. <sup>10</sup> Our results indicate that distortion does not influence the ability of the cation to accept electrons from a Lewis base, or its polarizability, but rather relieves the penalty associated with complex formation ( $\Delta E_{GD,Ti}$ ) and enhances  $\Delta E_{FRZ}$  which includes a complex interplay between permanent electrostatic charges, Pauli-repulsion, and dispersion interactions. <sup>29</sup> Since  $\Delta E_{POL}$  and  $\Delta E_{CT}$  are not dependent on facet area, this suggests that these terms depend largely on the adsorbate (for a given SSMC). Thus, we posit that shifts in the y-intercept of  $\Delta E_{POL}$  and  $\Delta E_{CT}$  will depend on the adsorbate polarizability and ionization energy.

Finally, we performed EDA calculations to investigate why the silsesquioxane model underbinds relative to experiments and QM/MM predictions (see red datapoint on Figure 9D). As shown in Figure S32, the EDA components for the silsesquioxane-pyridine complex are all smaller in magnitude than predictions based on the  $\equiv$ Ti-OH facet area. The most significant error resides in the  $\Delta E_{FRZ}$  (31.7% of total absolute error), followed by  $\Delta E_{POL}$  (21.1%),  $\Delta E_{GD,Ti}$  (20.8%),  $\Delta E_{CT}$  (18.6%), and  $\Delta E_{GD,Py}$  (7.8%). Thus, the errors associated with using a small cluster model are distributed relatively evenly amongst all the components of the intermolecular interactions. This further supports the need to use more extensive representations of the silica surrounding the active site to capture all interactions present in adsorption events. Since the first step in heterogeneously catalyzed reactions involves adsorption, we believe the errors pointed out here for adsorption may also translate to computational catalysis studies.

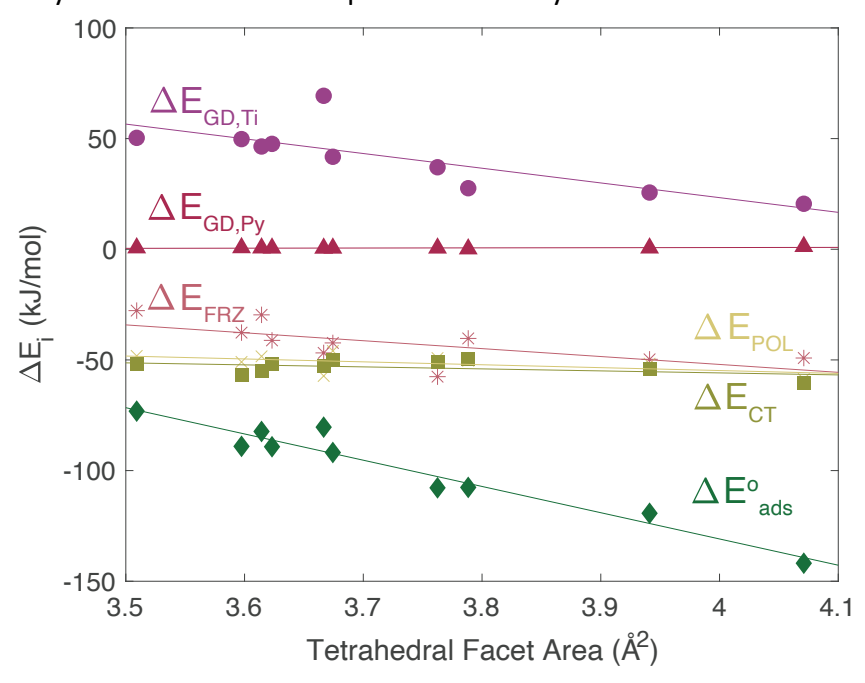


Figure 10: The dependence of each component of the EDA on the tetrahedral facet area.

Table 5: Linear fit parameters for lines in figure 10

EDA Component	Slope	Intercept	
$\Delta E_{GD,Ti}$	-66.5	289.2	
$\Delta E_{GD,Py}$	0.7	-2.1	
$\Delta E_{FRZ}$	-35.7	78.4	
$\Delta E_{POL}$	-13.1	-2.4	
$\Delta E_{CT}$	-9.1	-19.5	
$\Delta E_{ads}^o$	-118.6	343.5	

# Conclusions

This study has successfully developed and validated experimental and theoretical methods for determining enthalpies of adsorption for polar molecules interacting with ≡Si-OH and ≡Ti-OH sites located on the surface of amorphous silica. We showed that adsorbate coverage of ≡Si-OH groups can be determined accurately by IR spectrocsopy, and that enthalpies of adsorption obtained by fitting a Langmuir isotherm to these data agrees well with microcalorimetric measurements reported in the literature. We also have demonstrated that a silsesquioxane representation of ≡Si-OH sites is not large enough to capture non-local interactions between adsorbates and the surrounding silica support, resulting in consistent underestimation of the enthalpies of adsorption for polar molecules interacting with ≡Si-OH and ≡Ti-OH groups. By contrast, estimates of the enthalpy of adsorption on such sites that agree to within 10% of experimental measurements can be achieved using a QM/MM approach in which a given ≡Si-OH site is surrounded by amorphous silica to a radius of more than 11 Å. Extending our validated IR methods to ≡Ti-OH sites, we found that the isosteric enthalpy of adsorption of pyridine decreases with pyridine coverage for coverages up to 15% and then remains relatively constant (-105±10 kJ/mol) for coverages above 15%. Using our validated QM/MM model for ≡Si-OH sites, we generated a series of ≡Ti-OH sites differing in the degree of distortion of the tetrahedral facets (i.e., O-Ti-O triangular facets) and calculated the enthalpy of pyridine adsorption to each of them. We found that predicted enthalpy of pyridine adsorption is approximately proportional to the initial area of the ≡Ti-OH facet to which pyridine is bound. The prediction of the enthalpies of adsorption of pyridine for a tetrahedral facet area derived from experimental EXAFS measurements matches the value observed experimentally (-104±10 kJ/mol). This finding and the observation of an intense XANES pre-edge feature suggest that most ≡Ti-OH sites are symmetrical tetrahedrons and exhibit geometries consistent with those determined from EXAFS fitting. A small portion (<15%) of ≡Ti-OH sites are could be described as distorted and exhibit tetrahedral facet areas larger than those measured by EXAFS. This distortion causes a decrease in intensity of the pre-edge XANES features relative to a strictly tetrahedral standard (Ti[OSiPh₃]₄). Energy decomposition analysis (EDA) indicates that a large initial ≡Ti-OH site facet area increases the enthalpy of pyridine adsorption by reducing the geometric distortion penalty for the =Ti-OH site to achieve its optimized geometry in the adsorbate-bound complex and enhances frozen interactions (a component that comprises a complex interplay between permanent electrostatics, Pauli-repulsion, and dispersion). EDA calculations suggest distorted sites could exhibit tetrahedral facet areas as large as 4.35 Å<sup>2</sup> (as opposed to 3.76 Å<sup>2</sup> determined from EXAFS). The identification of distorted ≡Ti-OH sites opens up the need to consider the role

of such sites in the promotion of reactions catalyzed by ≡Ti-OH groups, which have previously been considered to be largely minimally distorted tetrahedra, as inferred from EXAFS data.

# Acknowledgments

This work was supported by the Office of Science, Office of Basic Energy Sciences of the U.S. Department of Energy under Contract No. DE-AC02-05CH11231. Work on energy decomposition analysis was supported by the U.S. National Science Foundation through Grant No. CHE-2313791. The authors thank Abraham Martinez for assistance with the acquisition of the TGA data in this work. The authors also acknowledge Dr. Yujia Ding for help acquiring XAS data, and Dr. Jeremy Kropf and Dr. Jacklyn Hall for assistance setting up the in-situ XAS cube reactor. This research used resources of the Advanced Photon Source; a U.S. Department of Energy (DOE) Office of Science User Facility operated for the DOE Office of Science by Argonne National Laboratory under Contract No. DE-AC02-06CH11357. MRCAT operations are supported by the Department of Energy and the MRCAT member institutions.

## References

- (1) Gao, X.; Wachs, I. E. Titania–Silica as Catalysts: Molecular Structural Characteristics and Physico-Chemical Properties. *Catalysis Today* **1999**, *51* (2), 233–254. https://doi.org/10.1016/S0920-5861(99)00048-6.
- (2) McDaniel, M. P. A Review of the Phillips Chromium Catalyst for Ethylene Polymerization. In *Handbook of Transition Metal Polymerization Catalysts*; Hoff, R., Ed.; John Wiley & Sons, Inc.: Hoboken, NJ, USA, 2018; pp 401–571. https://doi.org/10.1002/9781119242277.ch13.
- (3) Gani, T. Z. H.; Berkson, Z. J.; Zhu, R.; Kang, J. H.; Di Iorio, J. R.; Chan, K. W.; Consoli, D. F.; Shaikh, S. K.; Copéret, C.; Román-Leshkov, Y. Promoting Active Site Renewal in Heterogeneous Olefin Metathesis Catalysts. *Nature* **2023**, *617* (7961), 524–528. https://doi.org/10.1038/s41586-023-05897-w.
- (4) Ewing, C. S.; Bagusetty, A.; Patriarca, E. G.; Lambrecht, D. S.; Veser, G.; Johnson, J. K. Impact of Support Interactions for Single-Atom Molybdenum Catalysts on Amorphous Silica. *Ind. Eng. Chem. Res.* **2016**, *55* (48), 12350–12357. https://doi.org/10.1021/acs.iecr.6b03558.
- (5) Shylesh, S.; Bettinson, L. A.; Aljahri, A.; Head-Gordon, M.; Bell, A. T. Experimental and Computational Studies of Carbon–Carbon Bond Formation via Ketonization and Aldol Condensation over Site-Isolated Zirconium Catalysts. ACS Catal. 2020, 10 (8), 4566–4579. https://doi.org/10.1021/acscatal.9b05176.
- (6) Hanna, D. G.; Shylesh, S.; Li, Y.-P.; Krishna, S.; Head-Gordon, M.; Bell, A. T. Experimental and Theoretical Study of *n* -Butanal Self-Condensation over Ti Species Supported on Silica. *ACS Catal.* **2014**, *4* (9), 2908–2916. https://doi.org/10.1021/cs500704b.
- (7) Tiozzo, C.; Bisio, C.; Carniato, F.; Gallo, A.; Scott, S. L.; Psaro, R.; Guidotti, M. Niobium–Silica Catalysts for the Selective Epoxidation of Cyclic Alkenes: The Generation of the Active Site by Grafting Niobocene Dichloride. *Phys. Chem. Chem. Phys.* **2013**, *15* (32), 13354. https://doi.org/10.1039/c3cp51570b.
- (8) Thornburg, N. E.; Nauert, S. L.; Thompson, A. B.; Notestein, J. M. Synthesis–Structure–Function Relationships of Silica-Supported Niobium(V) Catalysts for Alkene Epoxidation with H <sub>2</sub> O <sub>2</sub>. *ACS Catal.* **2016**, *6* (9), 6124–6134. https://doi.org/10.1021/acscatal.6b01796.
- (9) Wachs, I. E. Catalysis Science of Supported Vanadium Oxide Catalysts. *Dalton Trans.* **2013**, 42 (33), 11762. https://doi.org/10.1039/c3dt50692d.
- (10) Caricato, M. Cluster Model Simulations of Metal-Doped Amorphous Silicates for Heterogeneous Catalysis. *J. Phys. Chem. C* **2021**, *125* (50), 27509–27519. https://doi.org/10.1021/acs.jpcc.1c07524.
- (11) Goldsmith, B. R.; Peters, B.; Johnson, J. K.; Gates, B. C.; Scott, S. L. Beyond Ordered Materials: Understanding Catalytic Sites on Amorphous Solids. *ACS Catal.* **2017**, *7* (11), 7543–7557. https://doi.org/10.1021/acscatal.7b01767.
- (12) Liu, C.; Camacho-Bunquin, J.; Ferrandon, M.; Savara, A.; Sohn, H.; Yang, D.; Kaphan, D. M.; Langeslay, R. R.; Ignacio-de Leon, P. A.; Liu, S.; Das, U.; Yang, B.; Hock, A. S.; Stair, P. C.; Curtiss, L. A.; Delferro, M. Development of Activity—Descriptor Relationships for Supported Metal Ion Hydrogenation Catalysts on Silica. *Polyhedron* **2018**, *152*, 73–83. https://doi.org/10.1016/j.poly.2018.06.006.

- (13) Patel, P.; Lu, Z.; Jafari, M. G.; Hernández-Prieto, C.; Zatsepin, P.; Mindiola, D. J.; Kaphan, D. M.; Delferro, M.; Kropf, A. J.; Liu, C. Integrated Experimental and Computational K-Edge X-Ray Absorption Near-Edge Structure Analysis of Vanadium Catalysts. *J. Phys. Chem. C* 2022, 126 (29), 11949–11962. https://doi.org/10.1021/acs.jpcc.2c02049.
- (14) Patel, P.; Wells, R. H.; Kaphan, D. M.; Delferro, M.; Skodje, R. T.; Liu, C. Computational Investigation of the Role of Active Site Heterogeneity for a Supported Organovanadium(III) Hydrogenation Catalyst. ACS Catal. 2021, 11 (12), 7257–7269. https://doi.org/10.1021/acscatal.1c00688.
- (15) Wells, R. H.; An, S.; Patel, P.; Liu, C.; Skodje, R. T. Single-Molecule Kinetics of Styrene Hydrogenation on Silica-Supported Vanadium: The Role of Disorder for Single-Atom Catalysts. *J. Phys. Chem. C* **2021**, *125* (37), 20286–20300. https://doi.org/10.1021/acs.jpcc.1c04759.
- (16) Van der Mynsbrugge, J.; Bell, A. T. Challenges for the Theoretical Description of the Mechanism and Kinetics of Reactions Catalyzed by Zeolites. *Journal of Catalysis* **2021**, *404*, 832–849. https://doi.org/10.1016/j.jcat.2021.08.048.
- (17) Mansoor, E.; Van Der Mynsbrugge, J.; Head-Gordon, M.; Bell, A. T. Impact of Long-Range Electrostatic and Dispersive Interactions on Theoretical Predictions of Adsorption and Catalysis in Zeolites. *Catalysis Today* **2018**, *312*, 51–65. https://doi.org/10.1016/j.cattod.2018.02.007.
- (18) Kiselev, A. V.; Kuznetsov, B. V.; Lanin, S. N. Adsorption of Triethylamine and Water Vapor and the Modification of Silica Surface by Gaseous Trimethylchlorosilane. *Journal of Colloid and Interface Science* **1979**, *69* (1), 148–156. https://doi.org/10.1016/0021-9797(79)90089-4.
- (19) Kuznetsov, B. V.; Tuan, N. A.; Rachmanova, T. A. Calorimetric and Isosteric Heats of Adsorption of Substances with Molecules of Different Electronic Structure. *Adsorption Science & Technology* **1989**, *6* (1), 27–34. https://doi.org/10.1177/026361748900600104.
- (20) Curthoys, G.; Davydov, V. Y.; Kiselev, A. V.; Kiselev, S. A.; Kuznetsov, B. V. Hydrogen Bonding in Adsorption on Silica. *Journal of Colloid and Interface Science* **1974**, *48* (1), 58–72. https://doi.org/10.1016/0021-9797(74)90328-2.
- (21) Cardonamartinez, N. Acid Strength of Silica-Alumina and Silica Studied by
   Microcalorimetric Measurements of Pyridine Adsorption. *Journal of Catalysis* 1990, 125

   (2), 427–444. https://doi.org/10.1016/0021-9517(90)90316-C.
- (22) Hertl, W.; Hair, M. L. Hydrogen Bonding between Adsorbed Gases and Surface Hydroxyl Groups on Silica. *J. Phys. Chem.* **1968**, *72* (13), 4676–4682. https://doi.org/10.1021/j100859a053.
- (23) Armandi, M.; Bolis, V.; Bonelli, B.; Otero Areán, C.; Ugliengo, P.; Garrone, E. Silanol-Related and Unspecific Adsorption of Molecular Ammonia on Highly Dehydrated Silica. *J. Phys. Chem. C* **2011**, *115* (47), 23344–23353. https://doi.org/10.1021/jp206301c.
- (24) Day, R. E.; Kiselev, A. V.; Kuznetsov, B. V. Non-Specific, Specific Molecular and Chemical Adsorption of Tetrahydrofuran on Progressively Dehydroxylated Aerosilogel. *Trans. Faraday Soc.* **1969**, *65*, 1386. https://doi.org/10.1039/tf9696501386.
- (25) Jarupatrakorn, J.; Tilley, T. D. Silica-Supported, Single-Site Titanium Catalysts for Olefin Epoxidation. A Molecular Precursor Strategy for Control of Catalyst Structure. *J. Am. Chem. Soc.* **2002**, *124* (28), 8380–8388. https://doi.org/10.1021/ja0202208.

- (26) Noh, G.; Lam, E.; Bregante, D. T.; Meyet, J.; Šot, P.; Flaherty, D. W.; Copéret, C. Lewis Acid Strength of Interfacial Metal Sites Drives CH <sub>3</sub> OH Selectivity and Formation Rates on Cu-Based CO <sub>2</sub> Hydrogenation Catalysts. *Angew. Chem.* **2021**, *133* (17), 9736–9745. https://doi.org/10.1002/ange.202100672.
- (27) Bregante, D. T.; Thornburg, N. E.; Notestein, J. M.; Flaherty, D. W. Consequences of Confinement for Alkene Epoxidation with Hydrogen Peroxide on Highly Dispersed Group 4 and 5 Metal Oxide Catalysts. *ACS Catal.* **2018**, *8* (4), 2995–3010. https://doi.org/10.1021/acscatal.7b03986.
- (28) Grosso-Giordano, N. A.; Hoffman, A. S.; Boubnov, A.; Small, D. W.; Bare, S. R.; Zones, S. I.; Katz, A. Dynamic Reorganization and Confinement of Ti <sup>IV</sup> Active Sites Controls Olefin Epoxidation Catalysis on Two-Dimensional Zeotypes. *J. Am. Chem. Soc.* **2019**, *141* (17), 7090–7106. https://doi.org/10.1021/jacs.9b02160.
- (29) Horn, P. R.; Mao, Y.; Head-Gordon, M. Probing Non-Covalent Interactions with a Second Generation Energy Decomposition Analysis Using Absolutely Localized Molecular Orbitals. *Phys. Chem. Chem. Phys.* **2016**, *18* (33), 23067–23079. https://doi.org/10.1039/C6CP03784D.
- (30) Zhuravlev, L. T. The Surface Chemistry of Amorphous Silica. Zhuravlev Model. *Colloids and Surfaces A: Physicochemical and Engineering Aspects* **2000**, *173* (1–3), 1–38. https://doi.org/10.1016/S0927-7757(00)00556-2.
- (31) Maschmeyer, T.; Rey, F.; Sankar, G.; Thomas, J. M. Heterogeneous Catalysts Obtained by Grafting Metallocene Complexes onto Mesoporous Silica. *Nature* **1995**, *378* (6553), 159–162. https://doi.org/10.1038/378159a0.
- (32) Johnson, B. F. G.; Klunduk, M. C.; Martin, C. M.; Sankar, G.; Teate, S. J.; Meurig Thomas, J. The Preparation, Molecular Structure and Catalytic Relevance of Ti(OSiPh3)4 and Ti(OGePh3)4. *Journal of Organometallic Chemistry* **2000**, *596* (1–2), 221–225. https://doi.org/10.1016/S0022-328X(99)00744-5.
- (33) Getsoian, A. "Bean"; Zhai, Z.; Bell, A. T. Band-Gap Energy as a Descriptor of Catalytic Activity for Propene Oxidation over Mixed Metal Oxide Catalysts. *J. Am. Chem. Soc.* **2014**, *136* (39), 13684–13697. https://doi.org/10.1021/ja5051555.
- (34) Harris, J. W.; Cordon, M. J.; Di Iorio, J. R.; Vega-Vila, J. C.; Ribeiro, F. H.; Gounder, R. Titration and Quantification of Open and Closed Lewis Acid Sites in Sn-Beta Zeolites That Catalyze Glucose Isomerization. *Journal of Catalysis* **2016**, *335*, 141–154. https://doi.org/10.1016/j.jcat.2015.12.024.
- (35) Crocellà, V.; Cerrato, G.; Magnacca, G.; Morterra, C. Adsorption of Acetone on Nonporous and Mesoporous Silica. *J. Phys. Chem. C* **2009**, *113* (37), 16517–16529. https://doi.org/10.1021/jp903910n.
- (36) Ravel, B.; Newville, M. ATHENA, ARTEMIS, HEPHAESTUS: Data Analysis for X-Ray Absorption Spectroscopy Using IFEFFIT. J Synchrotron Rad 2005, 12 (4), 537–541. https://doi.org/10.1107/S0909049505012719.
- (37) Chai, J.-D.; Head-Gordon, M. Long-Range Corrected Hybrid Density Functionals with Damped Atom—Atom Dispersion Corrections. *Phys. Chem. Chem. Phys.* **2008**, *10* (44), 6615–6620. https://doi.org/10.1039/B810189B.

- (38) Mardirossian, N.; Head-Gordon, M. ωB97M-V: A Combinatorially Optimized, Range-Separated Hybrid, Meta-GGA Density Functional with VV10 Nonlocal Correlation. *J. Chem. Phys.* **2016**, *144* (21), 214110. https://doi.org/10.1063/1.4952647.
- (39) Mardirossian, N.; Head-Gordon, M. Thirty Years of Density Functional Theory in Computational Chemistry: An Overview and Extensive Assessment of 200 Density Functionals. *Molecular Physics* **2017**, *115* (19), 2315–2372. https://doi.org/10.1080/00268976.2017.1333644.
- (40) Dasgupta, S.; Herbert, J. M. Standard Grids for High-precision Integration of Modern Density Functionals: SG-2 and SG-3. *J. Comput. Chem.* **2017**, *38* (12), 869–882. https://doi.org/10.1002/jcc.24761.
- (41) Li, Y.-P.; Gomes, J.; Mallikarjun Sharada, S.; Bell, A. T.; Head-Gordon, M. Improved Force-Field Parameters for QM/MM Simulations of the Energies of Adsorption for Molecules in Zeolites and a Free Rotor Correction to the Rigid Rotor Harmonic Oscillator Model for Adsorption Enthalpies. J. Phys. Chem. C 2015, 119 (4), 1840–1850. https://doi.org/10.1021/jp509921r.
- (42) Grimme, S. Supramolecular Binding Thermodynamics by Dispersion-Corrected Density Functional Theory. *Chem. Eur. J.* **2012**, *18* (32), 9955–9964. https://doi.org/10.1002/chem.201200497.
- (43) Epifanovsky, E.; Gilbert, A. T. B.; Feng, X.; Lee, J.; Mao, Y.; Mardirossian, N.; Pokhilko, P.; White, A. F.; Coons, M. P.; Dempwolff, A. L.; Gan, Z.; Hait, D.; Horn, P. R.; Jacobson, L. D.; Kaliman, I.; Kussmann, J.; Lange, A. W.; Lao, K. U.; Levine, D. S.; Liu, J.; McKenzie, S. C.; Morrison, A. F.; Nanda, K. D.; Plasser, F.; Rehn, D. R.; Vidal, M. L.; You, Z.-Q.; Zhu, Y.; Alam, B.; Albrecht, B. J.; Aldossary, A.; Alguire, E.; Andersen, J. H.; Athavale, V.; Barton, D.; Begam, K.; Behn, A.; Bellonzi, N.; Bernard, Y. A.; Berquist, E. J.; Burton, H. G. A.; Carreras, A.; Carter-Fenk, K.; Chakraborty, R.; Chien, A. D.; Closser, K. D.; Cofer-Shabica, V.; Dasgupta, S.; de Wergifosse, M.; Deng, J.; Diedenhofen, M.; Do, H.; Ehlert, S.; Fang, P.-T.; Fatehi, S.; Feng, Q.; Friedhoff, T.; Gayvert, J.; Ge, Q.; Gidofalvi, G.; Goldey, M.; Gomes, J.; González-Espinoza, C. E.; Gulania, S.; Gunina, A. O.; Hanson-Heine, M. W. D.; Harbach, P. H. P.; Hauser, A.; Herbst, M. F.; Hernández Vera, M.; Hodecker, M.; Holden, Z. C.; Houck, S.; Huang, X.; Hui, K.; Huynh, B. C.; Ivanov, M.; Jász, Á.; Ji, H.; Jiang, H.; Kaduk, B.; Kähler, S.; Khistyaev, K.; Kim, J.; Kis, G.; Klunzinger, P.; Koczor-Benda, Z.; Koh, J. H.; Kosenkov, D.; Koulias, L.; Kowalczyk, T.; Krauter, C. M.; Kue, K.; Kunitsa, A.; Kus, T.; Ladjánszki, I.; Landau, A.; Lawler, K. V.; Lefrancois, D.; Lehtola, S.; Li, R. R.; Li, Y.-P.; Liang, J.; Liebenthal, M.; Lin, H.-H.; Lin, Y.-S.; Liu, F.; Liu, K.-Y.; Loipersberger, M.; Luenser, A.; Manjanath, A.; Manohar, P.; Mansoor, E.; Manzer, S. F.; Mao, S.-P.; Marenich, A. V.; Markovich, T.; Mason, S.; Maurer, S. A.; McLaughlin, P. F.; Menger, M. F. S. J.; Mewes, J.-M.; Mewes, S. A.; Morgante, P.; Mullinax, J. W.; Oosterbaan, K. J.; Paran, G.; Paul, A. C.; Paul, S. K.; Pavošević, F.; Pei, Z.; Prager, S.; Proynov, E. I.; Rák, Á.; Ramos-Cordoba, E.; Rana, B.; Rask, A. E.; Rettig, A.; Richard, R. M.; Rob, F.; Rossomme, E.; Scheele, T.; Scheurer, M.; Schneider, M.; Sergueev, N.; Sharada, S. M.; Skomorowski, W.; Small, D. W.; Stein, C. J.; Su, Y.-C.; Sundstrom, E. J.; Tao, Z.; Thirman, J.; Tornai, G. J.; Tsuchimochi, T.; Tubman, N. M.; Veccham, S. P.; Vydrov, O.; Wenzel, J.; Witte, J.; Yamada, A.; Yao, K.; Yeganeh, S.; Yost, S. R.; Zech, A.; Zhang, I. Y.; Zhang, X.; Zhang, Y.; Zuev, D.; Aspuru-Guzik, A.; Bell, A. T.; Besley, N. A.; Bravaya, K. B.; Brooks, B. R.; Casanova, D.; Chai, J.-D.; Coriani, S.; Cramer, C. J.;

- Cserey, G.; DePrince, A. E.; DiStasio, R. A.; Dreuw, A.; Dunietz, B. D.; Furlani, T. R.; Goddard, W. A.; Hammes-Schiffer, S.; Head-Gordon, T.; Hehre, W. J.; Hsu, C.-P.; Jagau, T.-C.; Jung, Y.; Klamt, A.; Kong, J.; Lambrecht, D. S.; Liang, W.; Mayhall, N. J.; McCurdy, C. W.; Neaton, J. B.; Ochsenfeld, C.; Parkhill, J. A.; Peverati, R.; Rassolov, V. A.; Shao, Y.; Slipchenko, L. V.; Stauch, T.; Steele, R. P.; Subotnik, J. E.; Thom, A. J. W.; Tkatchenko, A.; Truhlar, D. G.; Van Voorhis, T.; Wesolowski, T. A.; Whaley, K. B.; Woodcock, H. L.; Zimmerman, P. M.; Faraji, S.; Gill, P. M. W.; Head-Gordon, M.; Herbert, J. M.; Krylov, A. I. Software for the Frontiers of Quantum Chemistry: An Overview of Developments in the Q-Chem 5 Package. *J. Chem. Phys.* **2021**, *155* (8), 084801. https://doi.org/10.1063/5.0055522.
- (44) Schweitzer, N. M.; Hu, B.; Das, U.; Kim, H.; Greeley, J.; Curtiss, L. A.; Stair, P. C.; Miller, J. T.; Hock, A. S. Propylene Hydrogenation and Propane Dehydrogenation by a Single-Site Zn <sup>2+</sup> on Silica Catalyst. *ACS Catal.* **2014**, *4* (4), 1091–1098. https://doi.org/10.1021/cs401116p.
- (45) Gierada, M.; Petit, I.; Handzlik, J.; Tielens, F. Hydration in Silica Based Mesoporous Materials: A DFT Model. *Phys. Chem. Chem. Phys.* **2016**, *18* (48), 32962–32972. https://doi.org/10.1039/C6CP05460A.
- (46) Tielens, F.; Gierada, M.; Handzlik, J.; Calatayud, M. Characterization of Amorphous Silica Based Catalysts Using DFT Computational Methods. *Catalysis Today* **2020**, *354*, 3–18. https://doi.org/10.1016/j.cattod.2019.03.062.
- (47) Parry, E. An Infrared Study of Pyridine Adsorbed on Acidic Solids. Characterization of Surface Acidity. *Journal of Catalysis* **1963**, *2* (5), 371–379. https://doi.org/10.1016/0021-9517(63)90102-7.
- (48) Jystad, A.; Leblanc, H.; Caricato, M. Surface Acidity Characterization of Metal-Doped Amorphous Silicates via Py-FTIR and <sup>15</sup> N NMR Simulations. *J. Phys. Chem. C* **2020**, *124* (28), 15231–15240. https://doi.org/10.1021/acs.jpcc.0c03292.
- (49) Suib, S. L.; Přech, J.; Szaniawska, E.; Čejka, J. Recent Advances in Tetra- (Ti, Sn, Zr, Hf) and Pentavalent (Nb, V, Ta) Metal-Substituted Molecular Sieve Catalysis. *Chem. Rev.* **2023**, *123* (3), 877–917. https://doi.org/10.1021/acs.chemrev.2c00509.
- (50) Child, M. J.; Heywood, M. J.; Pulton, S. K.; Vicary, G. A.; Geok Hua Yong; Rochester, C. H. Infrared Studies of the Adsorption of Triethylamine on Silica at the Solid/Vapor and Solid/Liquid Interfaces. *Journal of Colloid and Interface Science* **1982**, *89* (1), 202–208. https://doi.org/10.1016/0021-9797(82)90133-3.
- (51) Bregante, D. T.; Johnson, A. M.; Patel, A. Y.; Ayla, E. Z.; Cordon, M. J.; Bukowski, B. C.; Greeley, J.; Gounder, R.; Flaherty, D. W. Cooperative Effects between Hydrophilic Pores and Solvents: Catalytic Consequences of Hydrogen Bonding on Alkene Epoxidation in Zeolites. J. Am. Chem. Soc. 2019, 141 (18), 7302–7319. https://doi.org/10.1021/jacs.8b12861.
- (52) Sushkevich, V. L.; Vimont, A.; Travert, A.; Ivanova, I. I. Spectroscopic Evidence for Open and Closed Lewis Acid Sites in ZrBEA Zeolites. *J. Phys. Chem. C* **2015**, *119* (31), 17633–17639. https://doi.org/10.1021/acs.jpcc.5b02745.
- (53) Linstrom, P. NIST Chemistry WebBook, NIST Standard Reference Database 69, 1997. https://doi.org/10.18434/T4D303.
- (54) Kachurovskaya, N. A.; Zhidomirov, G. M.; Aristov, Y. I. On the Problem of Differentiation of Acetone Adsorption Species on the Silica Gel: Molecular Models of Adsorption Complexes.

- *Journal of Molecular Catalysis A: Chemical* **2000**, *158* (1), 281–285. https://doi.org/10.1016/S1381-1169(00)00091-1.
- (55) Zhang, K.; Caricato, M. Modeling Catalyzed Reactions on Metal-Doped Amorphous Silicates: The Case of Niobium-Catalyzed Ethylene Epoxidation. *J. Phys. Chem. C* **2023**, *127* (10), 4984–4997. https://doi.org/10.1021/acs.jpcc.3c00213.
- (56) DiVerdi, J. A.; Kobayashi, T.; Maciel, G. E. Molecular Dynamics of Pyridine Adsorbed on the Silica Surface. *J. Phys. Chem. C* **2007**, *111* (16), 5982–5989. https://doi.org/10.1021/jp067353q.
- (57) Campbell, C. T.; Sellers, J. R. V. The Entropies of Adsorbed Molecules. *J. Am. Chem. Soc.* **2012**, *134* (43), 18109–18115. https://doi.org/10.1021/ja3080117.
- (58) Bukowski, B. C.; Bates, J. S.; Gounder, R.; Greeley, J. First Principles, Microkinetic, and Experimental Analysis of Lewis Acid Site Speciation during Ethanol Dehydration on Sn-Beta Zeolites. *Journal of Catalysis* **2018**, *365*, 261–276. https://doi.org/10.1016/j.jcat.2018.07.012.
- (59) Johnson, R. Computational Chemistry Comparison and Benchmark Database, NIST Standard Reference Database 101, 2002. https://doi.org/10.18434/T47C7Z.
- (60) Putnam, W. E.; McEachern, D. M.; Kilpatrick, J. E. Entropy and Related Thermodynamic Properties of Acetonitrile (Methyl Cyanide). *The Journal of Chemical Physics* **1965**, *42* (2), 749–755. https://doi.org/10.1063/1.1696002.
- (61) Westrum, E. F.; Ribner, A. Trimethylacetonitrile. Low-Temperature Heat Capacity, Vapor Pressure, and Chemical Thermodynamics of the Crystalline, Liquid, and Gaseous Phases. *J. Phys. Chem.* **1967**, *71* (5), 1216–1224. https://doi.org/10.1021/j100864a006.
- (62) Ratnasamy, P.; Srinivas, D.; Knözinger, H. Active Sites and Reactive Intermediates in Titanium Silicate Molecular Sieves. In *Advances in Catalysis*; Elsevier, 2004; Vol. 48, pp 1–169. https://doi.org/10.1016/S0360-0564(04)48001-8.
- (63) Yamamoto, T. Assignment of Pre-Edge Peaks in K-Edge x-Ray Absorption Spectra of 3d Transition Metal Compounds: Electric Dipole or Quadrupole? *X-Ray Spectrom.* 2008, 37 (6), 572–584. https://doi.org/10.1002/xrs.1103.
- (64) Eaton, T. R.; Campos, M. P.; Gray, K. A.; Notestein, J. M. Quantifying Accessible Sites and Reactivity on Titania–Silica (Photo)Catalysts: Refining TOF Calculations. *Journal of Catalysis* **2014**, *309*, 156–165. https://doi.org/10.1016/j.jcat.2013.09.015.
- (65) Farges, F.; Brown, G. E.; Rehr, J. J. Ti K -Edge XANES Studies of Ti Coordination and Disorder in Oxide Compounds: Comparison between Theory and Experiment. *Phys. Rev. B* 1997, 56 (4), 1809–1819. https://doi.org/10.1103/PhysRevB.56.1809.
- (66) Demmelmaier, C. A.; White, R. E.; Van Bokhoven, J. A.; Scott, S. L. Evidence for a Chromasiloxane Ring Size Effect in Phillips (Cr/SiO2) Polymerization Catalysts. *Journal of Catalysis* **2009**, *262* (1), 44–56. https://doi.org/10.1016/j.jcat.2008.11.024.
- (67) De Clercq, R.; Dusselier, M.; Poleunis, C.; Debecker, D. P.; Giebeler, L.; Oswald, S.; Makshina, E.; Sels, B. F. Titania-Silica Catalysts for Lactide Production from Renewable Alkyl Lactates: Structure—Activity Relations. ACS Catal. 2018, 8 (9), 8130–8139. https://doi.org/10.1021/acscatal.8b02216.
- (68) Gao, X.; Bare, S. R.; Fierro, J. L. G.; Banares, M. A.; Wachs, I. E. Preparation and In-Situ Spectroscopic Characterization of Molecularly Dispersed Titanium Oxide on Silica. *J. Phys. Chem. B* **1998**, *102* (29), 5653–5666. https://doi.org/10.1021/jp981423e.

- (69) Zaki, M. I.; Hasan, M. A.; Al-Sagheer, F. A.; Pasupulety, L. In Situ FTIR Spectra of Pyridine Adsorbed on SiO2–Al2O3, TiO2, ZrO2 and CeO2: General Considerations for the Identification of Acid Sites on Surfaces of Finely Divided Metal Oxides. *Colloids and Surfaces A: Physicochemical and Engineering Aspects* **2001**, *190* (3), 261–274. https://doi.org/10.1016/S0927-7757(01)00690-2.
- (70) Cordon, M. J.; Harris, J. W.; Vega-Vila, J. C.; Bates, J. S.; Kaur, S.; Gupta, M.; Witzke, M. E.; Wegener, E. C.; Miller, J. T.; Flaherty, D. W.; Hibbitts, D. D.; Gounder, R. Dominant Role of Entropy in Stabilizing Sugar Isomerization Transition States within Hydrophobic Zeolite Pores. J. Am. Chem. Soc. 2018, 140 (43), 14244–14266. https://doi.org/10.1021/jacs.8b08336.
- (71) Zholobenko, V.; Freitas, C.; Jendrlin, M.; Bazin, P.; Travert, A.; Thibault-Starzyk, F. Probing the Acid Sites of Zeolites with Pyridine: Quantitative AGIR Measurements of the Molar Absorption Coefficients. *Journal of Catalysis* **2020**, *385*, 52–60. https://doi.org/10.1016/j.jcat.2020.03.003.
- (72) Grosso-Giordano, N. A.; Zones, S. I.; Katz, A. Opportunities for Controlling Catalysis by Designing Molecular Environments around Active Sites: Cations Supported on Amorphous versus Crystalline Zeolitic Silicate Supports. In Catalysis; Spivey, J., Han, Y.-F., Shekhawat, D., Eds.; Royal Society of Chemistry: Cambridge, 2019; Vol. 31, pp 72–126. https://doi.org/10.1039/9781788016971-00072.